Research Square

Preprints are preliminary reports that have not undergone peer review.
They should not be considered conclusive, used to inform clinical practice,
or referenced by the media as validated information.

The Emerging Heat-Drought Regime of The Barind Tract: Hydroclimatic Trends, Satellite Responses, And Projections To 2050

Fahim Shahriar Pranto

pfahimshahriar@gmail.com

University of Dhaka

Abdullah Osama Swaccho

Aston University

Article

Keywords: Drought, Heatwaves, Evapotranspiration, Remote Sensing, Compound Hazards, Getis-Ord Gi* Hotspot Analysis, Machine Learning, Barind Tract

Posted Date: November 18th, 2026

DOI: https://doi.org/10.21203/rs.3.rs-11589664/v1

License: This work is licensed under a Creative Commons Attribution 4.0 International License.
Read Full License

Additional Declarations: No competing interests reported.

The Emerging Heat-Drought Regime of The Barind Tract: Hydroclimatic Trends, Satellite Responses, And Projections To 2050

Fahim Shahriar Pranto[a,*], **Abdullah Osama Swaccho**[b]

[a] Institute of Disaster Management and Vulnerability Studies, University of Dhaka, Dhaka 1000, Bangladesh

[b] School of Engineering and Innovation, Aston University, Aston Triangle, Birmingham B4 7ET, United Kingdom

[*] *Corresponding author. E-mail address: pfahimshahriar@gmail.com*

Abstract

Compound heat-drought events threaten agricultural sustainability and water security across the Barind Tract in northwestern Bangladesh. This study examines meteorological drought dynamics, satellite-observed land-surface responses, compound risk, and mid-century hydroclimatic projections across Rajshahi District. We analysed 36 years of daily weather records (1990-2025) from Bangladesh Meteorological Department Station 41859, calculating the Standardised Precipitation Index and Standardised Precipitation Evapotranspiration Index across 1- to 24-month timescales against a fixed 1990-2005 baseline. Non-parametric Sen's slope and Mann-Kendall tests revealed significant annual warming in maximum temperature (+0.029 °C/year, $p = 0.0012$) and minimum temperature (+0.026 °C/year, $p < 0.001$), while reference evapotranspiration declined (-2.677 mm/year, $p = 0.0013$). Monsoon rainfall decreased by 10.055 mm/year ($p = 0.0137$), driving a long-term decline in 12-month water balance (-0.018/year, $p < 0.01$). We found 34 meteorological drought events, led by the extreme July-November 2010 episode. Satellite MODIS observations (2000-2025) showed rapid thermal coupling where land surface temperature anomalies at drought onset (Spearman RHO = -0.122 to -0.179 at lag 0), while evapotranspiration deficits lagged by 1 to 3 months. Bivariate Compound Heat-Drought Index mapping revealed significant hotspots covering 18.41% of the district, heavily concentrated across elevated clay terraces in mango orchards (25.50% of orchard area) and cropland (6.90%). Walk-forward validated machine-learning models reduced projection root mean square error by 32.0% to 85.5% over linear baselines, projecting continued warming with January 2050 maximum

temperatures reaching 26.43 °C. These empirical findings provide operational targets for groundwater governance, orchard heat protection, and local climate services.

Keywords: *Drought, Heatwaves, Evapotranspiration, Remote Sensing, Compound Hazards, Getis-Ord Gi* Hotspot Analysis, Machine Learning, Barind Tract*

Practical Implications

Agricultural producers, water managers, and public health officials in northwestern Bangladesh face a changing hydroclimatic hazard. In the Barind Tract, drought is no longer a simple rainfall deficit. It has evolved into an atmospheric compound hazard where intense summer warming coincides with severe soil moisture depletion. This chapter explains how regional institutions can use our findings to adjust operational decisions, invest in infrastructure, and allocate local resources.

Who can use these findings:

Four primary user groups require these results for operational planning. First, the Barind Multipurpose Development Authority and Department of Agricultural Extension can deploy the Upazila-level vulnerability rankings to target crop diversification and irrigation scheduling. Second, the Bangladesh Water Development Board and local upazila parishads can use the spatial hotspot maps to regulate deep tube well installations and design artificial aquifer recharge schemes. Third, disaster management committees can integrate satellite land surface temperature anomalies into early warning protocols. Fourth, the Ministry of Health and Family Welfare can anticipate seasonal heat stress among outdoor agricultural laborers.

Decisions Informed by Specific Results:

Every empirical finding in this study directly informs an operational decision. Our trend diagnostics establish that warming is heavily concentrated during the monsoon season, where maximum temperatures increase by 0.065 °C per year ($p < 0.001$) and minimum temperatures increase by 0.031 °C per year ($p < 0.001$). Concurrently, monsoon rainfall drops by 10.055 mm per year ($p = 0.0137$). Because the monsoon supplies 71.7% of total precipitation, farmers cannot assume rain-fed Aman rice will complete grain filling

without supplemental irrigation. Agronomists must schedule supplementary surface water storage for late monsoon dry spells rather than planning solely for pre-monsoon moisture shortages.

Our satellite biophysical analysis shows that surface thermal anomalies peak within one month of meteorological drought onset (Spearman correlation of -0.122 to -0.179 at lag 0). In contrast, evapotranspiration deficits and root-zone drying persist for two to three months after atmospheric drought breaks. This lag informs irrigation termination timing. Field managers who halt irrigation immediately when rainfall resumes risk exposing crops to severe subsoil moisture stress. Groundwater pumping and canal releases must continue through the two-month lag window until soil reservoirs are fully replenished.

At the spatial scale, Getis-Ord Gi* hotspot analysis reveals that compound heat-drought stress is not uniform across the district. Statistically significant hotspots occupy 18.41% of Rajshahi District (35,443 ha), clustering tightly on the elevated Pleistocene clay terraces of Godagari, Tanore, and Nachole. Stratification by land cover indicates that commercial mango orchards carry the highest exposure, with 25.50% of orchard area (33,476 ha) located within high-confidence hotspots. Cropland and paddy fields hold 6.90% of their area in hotspots (4,627 ha). Local authorities should concentrate financial subsidies for drip irrigation, micro-sprinklers, and orchard mulching in western Godagari and northern Tanore instead of scattering resources across low-risk eastern upazilas.

Practical field application: A worked advisory example

Consider a field officer in Godagari Upazila managing a 10-hectare commercial mango orchard during the dry pre-monsoon phase (March to May). Historically, daily maximum temperatures exceed 40 °C while rainfall averages only 231.5 mm across the entire three-month season. The underlying soil consists of weathered grey terrace clay with an infiltration capacity of only 2 to 3 mm per day and a restrictive plough pan at 6 to 8 cm depth. Regional groundwater extraction depends on 10,307 deep tube wells and 88,390 shallow tube wells, causing local water tables to fall rapidly.

Under our decision framework, when the 3-month Standardised Precipitation Evapotranspiration Index drops below -1.0, the officer does not wait for foliage to yellow. Satellite thermal anomalies detect canopy temperature four to six weeks before visible

desiccation occurs. The manager triggers three consecutive actions: (1) apply organic straw mulching across tree root zones to retard soil heat flux and conserve the thin 0.8% to 1.2% organic matter layer, (2) transition from flood irrigation to pulsed night-time drip applications, saving up to 40% of well water, and (3) excavate on-farm recharge trenches that penetrate the 14-meter clay mantle, capturing sudden heavy runoff when rainfall occurs.

Understanding uncertainty and technical boundaries

Practitioners must understand several analytical boundaries when applying these findings. Our forward projections to 2050 rely on walk-forward validated machine learning combining Random Forest regressors with non-parametric Sen's slope detrending. This framework assumes that historical warming rates and autoregressive dynamics continue along their observed trajectory. It does not simulate sudden greenhouse gas mitigation pathways or rapid shifts in regional monsoon circulation. If global carbon emissions diverge drastically from historical trends, actual mid-century temperatures will differ from our benchmark projections (such as January 2050 maximum temperatures of 26.43 °C).

Operational constraints also apply to MODIS Terra satellite observations. The 1 km resolution for land surface temperature and 500 m resolution for evapotranspiration cannot resolve individual smallholder plots smaller than 0.5 hectares. Cloud cover during the peak monsoon (June to September) occasionally obstructs optical passes, requiring composite time-series smoothing. Practitioners must verify regional satellite indicators against local in situ soil moisture probes and piezometer logs before enacting binding groundwater bans.

What these results do not show

This study models physical hazard exposure. It does not measure household socio-economic vulnerability, financial debt, access to credit, or farm-gate produce prices. A high biophysical hotspot does not automatically equal agricultural collapse if a farming community possesses deep financial reserves or alternative river water pumping. Local government agencies must combine our physical hazard maps with ward-level demographic surveys to identify genuinely vulnerable farming families.

Introduction

Climate change alters the frequency, duration, and severity of hydroclimatic extremes across South Asia. In monsoon-dependent agricultural basins, these impacts rarely occur in isolation. Low rainfall, elevated temperatures, and depleted soil moisture frequently coincide, producing damage that exceeds the impact of any single hazard (Calvin et al., 2023). Empirical analyses demonstrate that multivariate compound events cluster spatially rather than distributing uniformly across river basins (Ridder et al., 2020). Across Asian rice landscapes, concurrent heat and drought stress during reproductive phases reduces grain weight and triggers Spike let sterility (Rahman et al., 2022). In major agricultural plains, compound dry and hot events expand crop exposure over multi-decadal time horizons (Wang et al., 2025). As atmospheric temperatures climb and rainfall regimes shift, drought severity increasingly reflects atmospheric evaporative demand alongside rainfall deficits (Vicente-Serrano et al., 2020).

The Barind Tract in northwestern Bangladesh represents one of the most hydro climatically vulnerable farming regions in the Bengal Basin (Mou et al., 2023). Spanning 2,407 km² across nine Upazilas in Rajshahi District, the territory experiences a tropical wet-and-dry climate (Islam, 2013). Recent observational evidence identifies northwestern Bangladesh as a critical zone of agricultural vulnerability under shifting rainfall regimes (Das et al., 2023), (Kamruzzaman et al., 2022), and (Sultana et al., 2021). Elevated Pleistocene clay terraces cover roughly 160,000 ha, representing 21% of the wider physiographic unit. Pre-monsoon daily maximum temperatures routinely exceed 40 °C in May, while winter minimum temperatures fall to 6 °C in January. The underlying grey terrace soils exhibit low infiltration capacities of 2 to 3 mm per day, a dense plough pan at 6 to 8 cm depth, and low organic matter contents of 0.8% to 1.2% (Rashid et al., 2018). Mean annual precipitation ranges between 1,250 and 2,000 mm, falling well below the national average of 2,550 mm. Because a 14-meter Pleistocene clay layer chokes groundwater recharge, intensive boro rice and expanding mango orchards rely on 10,307 deep tube wells and 88,390 shallow tube wells (Hossain et al., 2025). Severe drought afflicted the region across more than 12% of months between 2010 and 2019, while extreme drought covered over 5% of the tract (Sadiq et al., 2023). Declining groundwater

tables and rising temperature extremes compound regional water scarcity (Sarker et al., 2026) and (Tahasin et al., 2023).

Drought monitoring in the Bengal Basin has traditionally relied on precipitation indices such as the Standardised Precipitation Index (McKee et al., 1993). While precipitation metrics track rainfall deficits, they omit temperature-driven changes in atmospheric evaporative demand. The Standardised Precipitation Evapotranspiration Index incorporates reference evapotranspiration, capturing combined thermal and moisture stress (Vicente-Serrano et al., 2010). The choice between these indices represents a fundamental methodological decision. Global evaluations show that index divergence forms the largest contributor to drought-hazard quantification uncertainty as warming progresses (Tabari et al., 2021). Regional evaluations in Bangladesh confirm that drought severity is reorganising spatially, with return periods lengthening in central and southern zones (Mamun et al., 2024). Station-based evaluations across the northwest demonstrate strong drought variability (Ferdous and Rashid, 2019). The Barind Tract serves as an instructive empirical test case because thermal warming is statistically pronounced while annual rainfall trends remain weak.

Meteorological indices do not capture how the land surface responds to atmospheric drying. Satellite remote sensing provides surface diagnostics at sub-district resolution. Moderate Resolution Imaging Spectroradiometer land surface temperature (MOD11A2) and evapotranspiration (MOD16A2) products resolve surface heating and vegetation water stress (Li et al., 2022), (Mu et al., 2011), and (Wan et al., 2015). Thermal anomalies serve as early indicators because plant water deficits alter stomatal regulation and leaf energy balance before tissue desiccation appears in optical bands (Hank et al., 2018). Globally, soil moisture governs ecosystem recovery across 58.4% of land area with a mean recovery time of 3.3 months (Ying et al., 2023). Soil moisture and atmospheric coupling operate non-linearly across critical moisture thresholds (Hsu and Dirmeyer, 2023). Land use and land cover alter surface albedo, aerodynamic roughness, and latent heat fluxes, creating distinct biophysical drought responses across cover types (Duveiller et al., 2018). Compound risk assessments must stratify hazard exposure by land use rather than treating the district as a homogeneous landscape.

Three research gaps remain open in the regional literature. First, compound heat-drought evaluations combining atmospheric anomalies with satellite biophysical metrics remain scarce below the divisional scale in Bangladesh (Rahman et al., 2026). Existing studies couple precipitation with thermal metrics but stop short of forward projections. Second, previous Barind studies depend on sparse synoptic records that obscure sub-district spatial heterogeneity, leaving multi-decadal variability unresolved across high-density grids (Esha et al., 2026). Third, regional climate projections rely on coarse general circulation model ensembles where structural uncertainty, emissions scenario selection, and downscaling biases exceed local adaptation planning signals (Lafferty and Sriver, 2023) and (Tebaldi et al., 2021). No study has integrated multi-decadal station trends, satellite biophysical response latencies, spatial compound risk mapping, and walk-forward validated empirical projections into a unified analytical framework for Rajshahi District.

This study addresses these gaps through four specific research objectives:

1. Characterise long-term trends (1990-2025) in rainfall, temperature, and reference evapotranspiration, quantifying multi-scalar drought regimes against a fixed 1990-2005 baseline.
2. Quantify satellite land-surface thermal and moisture responses to meteorological drought using MODIS anomalies, evaluating response latency and biophysical hysteresis.
3. Construct a bivariate Compound Heat-Drought Index, delineate statistically significant spatial hotspots using Getis-Ord Gi* statistics, and stratify compound risk across 2025 land-use classes.
4. Develop a walk-forward validated machine-learning framework combining Random Forest regressors with non-parametric detrending to project hydroclimatic variables and prediction intervals to 2050 under a continuation-of-trend assumption.

Study Area and Data

Study Area

Rajshahi District occupies 2,407 km² in northwestern Bangladesh, bounded by latitudes 24.12° N to 24.72° N and longitudes 88.28° E to 88.98° E (Fig. 11). The district comprises nine administrative Upazilas: Paba, Durgapur, Mohanpur, Charghat, Bagha, Godagari, Tanore, Puthia, and Bagmara. Geomorphologically, western and northern upazilas belong to the High Barind Tract, an uplifted Pleistocene terrace characterised by undulating topography, entrenching drainage channels, and acidic clay soils. Eastern and southern sectors transition into Recent alluvium along the Ganges (Padma) River floodplain. The terrace subsoil contains a dense, illuvial clay layer exceeding 14 m in thickness, restricting vertical percolation to 2-3 mm per day (Hossain et al., 2025). The regional climate is tropical monsoon. Mean annual precipitation totals 1,378.280 mm, with roughly 72% concentrated during the summer monsoon from June to September. Daily maximum temperatures exceed 40 °C during pre-monsoon dry spells, driving high evaporative demand across agricultural fields.

Meteorological Observations

Daily surface meteorological data spanning 1 January 1990 to 31 December 2025 (36 consecutive years, N = 432 months) were obtained from the Bangladesh Meteorological Department central synoptic station at Rajshahi (BMD Station 41859, Lat 24.37° N, Lon 88.60° E, elevation 19.5 m above sea level). The observational record contains six primary surface variables: daily precipitation (P, mm), maximum temperature (Tmax, °C), minimum temperature (Tmin, °C), relative humidity (RH, %), bright sunshine duration (n, hours per day), and 2 m horizontal wind speed (u_2, m/s). Quality control screening confirmed that data completeness exceeded 99.9% with fewer than 0.1% missing entries across the 36-year sequence. Missing values were gap-filled using mean values from adjacent days. No monthly interval was excluded from statistical trend calculations or drought index derivations. Station 41859 provides the only continuous, long-term synoptic time series within the district, ensuring internal physical consistency across all computed atmospheric water-balance components.

Satellite Remote Sensing and Land-Cover Data

Satellite observations spanning February 2000 to December 2025 (25 years, N = 300 months) were extracted from NASA MODIS Collection 6.1 platforms via Google Earth Engine. Daytime Land Surface Temperature was extracted from the MOD11A2 8-day composite product at 1 km spatial resolution (Wan et al., 2015). Terrestrial Evapotranspiration was acquired from the MOD16A2 8-day composite product at 500 m spatial resolution (Mu et al., 2011). Quality assessment bands were screened to eliminate cloud-contaminated pixels, achieving a 0.000% low-quality flag rate across the final analytical dataset. The 8-day images were aggregated into calendar-month means for each of the nine Upazilas using official administrative boundaries.

Land use and land cover for 2025 were classified across the district at 30 m resolution using multi-seasonal Sentinel-2 surface reflectance imagery. The classification delineates five primary classes: Forest/Tree Cover (Class 1, 7,748.5 ha), Built-up/Urban (Class 2, 7,257.2 ha), Cropland/Paddy (Class 3, 67,060.7 ha), Mango Orchards (Class 4, 131,278.5 ha), and Bare/Fallow (Class 5, 182.5 ha). These classes separate perennial tree canopies from seasonal grain fields, allowing differentiated evaluations of biophysical surface stress (Duveiller et al., 2018) and (Faridatul and Ahmed, 2020).

Methods

Reference for Evapotranspiration and Meteorological Drought Indices

Monthly reference evapotranspiration (ET_0) was calculated using the standardised FAO-56 Penman-Monteith formulation (Allen et al., 1998):

where ET_0 is reference evapotranspiration(mm/day), R n is net radiation at the crop surface (MJ/m²/day), G is soil heat flux density (MJ/m²/day), T is mean daily air temperature at 2 m height (°C), u_2 is wind speed at 2 m height (m/s), e s is saturation vapour pressure (kPa), e a is actual vapour pressure (kPa), Δ is the slope of the vapour pressure curve (kPa/°C), and γ is the psychrometric constant (kPa/°C).

Non-parametric trend detection across all hydroclimatic time series was conducted using the Mann-Kendall test (Mann, 1945) and Sen's slope estimator (Sen, 1968). Meteorological drought regimes were quantified using the Standardised Precipitation

Index (SPI) and the Standardised Precipitation Evapotranspiration Index (SPEI) at 1-, 3-, 6-, 12-, and 24-month accumulation scales. For SPI, monthly rainfall totals were fitted to a two-parameter gamma distribution (McKee et al., 1993):

where α is the shape parameter, β is the scale parameter, and Γ(α) is the gamma function. For SPEI, the climatic water balance $D = P - ET_0$ was fitted to a three-parameter log-logistic distribution (Vicente-Serrano et al., 2010). Severity classifications followed established thresholds: Moderate (-1.00 to -1.49), Severe (-1.50 to -1.99), and Extreme (≤ -2.00) (Hashim et al., 2017). Both indices were calibrated against a fixed historical baseline from 1990 to 2005 (16 years, 192 months). This fixed climatological baseline prevents shifting normal conditions from masking progressive multi-decadal drying trends.

Land-Surface Biophysical Response and Latency

Monthly MODIS LST and ET composites were converted into deseasonalised z-score anomalies per Upazila:

where X {i,m} is the observed metric in year ‘i’ and month ‘m’, while μ m and σ m denote the climatological mean and standard deviation for calendar month m across the 2000-2025 satellite baseline. Deseasonalisation removes the dominant annual solar cycle, isolating interannual surface anomalies driven by moisture stress.

Biophysical response latency was evaluated using cross-correlation functions between SPEI-3 and satellite anomalies (z-LST and z-ET) across lags k = 0 to 3 months. To evaluate composite land-surface recovery dynamics, superposed epoch analysis was conducted across the five most severe satellite-era drought episodes (July-November 2010, August-November 2018, June-August 2023, November-December 2014, and July-August 2022). Upazila anomalies were aligned relative to drought peak months (τ = 0) across an eleven-month window spanning τ = -4 to +6 months, reporting composite means, standard errors, and two-sided Student's t-test significance values.

Compound Heat-Drought Index and Spatial Hotspot Analysis

To capture simultaneous thermal and moisture stress, a bivariate Compound Heat-Drought Index was formulated:

where z-LST is the standardised surface temperature anomaly and z-ET is the standardised evapotranspiration anomaly. Inverting the sign of z-ET ensures that moisture deficits contribute positively to compound stress. The formulation assigns equal weights of 0.5 to thermal and evaporative anomalies, treating both physical dimensions symmetrically. To prevent mathematical double counting, CHDI relies exclusively on satellite observations, avoiding atmospheric ET_0 terms that already enter SPEI-3.

Spatial clustering of CHDI was evaluated using Getis-Ord Gi* statistics with rook-adjacency spatial weight matrices across the 30 m raster domain. Pixels with $Z > 1.96$ were classified as statistically significant hotspots at $p < 0.05$, reporting confidence tiers at 90% ($p < 0.10$), 95% ($p < 0.05$), and 99% ($p < 0.01$). Gi* statistics identify localized dependence structures that global Moran's I statistics miss (Getis and Ord, 1992). Hotspot maps were overlaid on the 2025 land-cover layer to determine differential hazard exposure across farming systems.

Machine-Learning Projections to 2050

Mid-century projections to 2050 were developed using a walk-forward validated machine-learning pipeline. Tree-based models offer robust forecasting in hydroclimatic regimes (Elbeltagi et al., 2022), while support-vector structures handle multi-feature meteorological inputs effectively (Alshahrani et al., 2024). Models were trained on historical records from 1990 to 2015 and evaluated on an independent test window from 2016 to 2025. Random Forest regressors (Breiman, 2001) were trained on three autoregressive lag features (lag 1, lag 2, lag 3), calendar month, and a linear time index, benchmarked against a non-parametric Theil-Sen linear trend baseline (Sen, 1968). Feature importance evaluations indicated that the time index contributed less than 5% to explained variance for temperature and evapotranspiration (0.021 for Tmax, 0.007 for Tmin, and 0.024 for ET_0). Consequently, a detrend-first architecture was implemented: long-term Sen's slope trends were extracted, residual variations were modelled with Random Forest, and linear trends were re-added during 2050 extrapolation. Prediction

intervals at 90% confidence were generated via 1,000 bootstrap iterations (Hyndman and Athanasopoulos, 2021).

A stationarity fallback rule was applied to non-trending series. Because annual rainfall exhibited a flat Theil-Sen slope (0.000 mm/month) and non-significant Mann-Kendall test ($p = 0.066$), machine-learning projections collapsed to constant mean residuals once autoregressive lags were filled. Rainfall was therefore projected as a monthly climatological baseline derived from historical training data with bootstrap prediction intervals. Forward trajectories represent statistical continuation-of-trend projections rather than dynamic emissions scenarios, preserving local observational fidelity over scenario uncertainty (Lafferty and Sriver, 2023).

Computational Workflow

All data processing, spatial analyses, and statistical modelling were executed in Python 3.14 and R 4.3 using libraries rasterio, geopandas, pysal, scikit-learn, and statsmodels. Satellite extraction was performed using Google Earth Engine. The analytical pipeline followed a strict linear sequence: meteorological quality control, baseline index calibration, satellite standardization, lagged response analysis, CHDI derivation, spatial hotspot classification, and detrended machine-learning projection.

Results

Long-Term Hydroclimatic Trends and Meteorological Drought Dynamics (1990-2025)

Over the 36-year synoptic record, Rajshahi District received a mean annual precipitation of 1,378.280 mm (standard deviation SD = 278.940 mm, coefficient of variation CV = 20.200%), with daily maximum temperatures averaging 31.470 °C and minimum temperatures averaging 20.690 °C (Table 1.1). Reference evapotranspiration averaged 1,255.300 mm annually (SD = 45.770 mm). Seasonal breakdowns demonstrate high rainfall concentration: the summer monsoon (June-September or JJAS) delivered 988.530 mm (71.72% of total, Table 1.3), pre-monsoon (March-May or MAM) contributed

231.470 mm (16.79%, Table 1.2), and winter (October-February or ONDJF) supplied 158.280 mm (11.48%, Table 1.4). Pre-monsoon conditions exhibited the highest evaporative demand, with ET_0 totalling 412.950 mm across three months amidst high sunshine duration (7.580 h/day) and low relative humidity (70.600%).

Non-parametric trend analysis (Table 2, Fig. 1) revealed statistically significant annual warming in both Tmax (+0.029 °C/year, Z = 3.240, p = 0.0012) and Tmin (+0.026 °C/year, Z = 4.060, p < 0.001). Seasonal disaggregation showed that warming was concentrated primarily during the monsoon season: JJAS Tmax climbed by +0.065 °C/year (Z = 5.200, p < 0.001) and JJAS Tmin rose by +0.031 °C/year (Z = 5.250, p < 0.001). Winter Tmin also warmed significantly (+0.021 °C/year, p = 0.0199). In contrast, annual reference evapotranspiration exhibited a statistically significant downward trend (-2.677 mm/year, Z = -3.210, p = 0.0013), driven by pronounced declines during pre-monsoon (-1.240 mm/year, p = 0.0001) and winter (-1.286 mm/year, p < 0.001) periods. Annual rainfall displayed a weak, non-significant decline (-8.619 mm/year, Z = -1.840, p = 0.0659), masking divergent seasonal trajectories: monsoon rainfall decreased significantly by -10.055 mm/year (Z = -2.470, p = 0.0137), while pre-monsoon rainfall increased by +2.080 mm/year (Z = 2.390, p = 0.0170).

Multi-scalar drought characterization using SPEI-3 identified 34 distinct drought events (SPEI-3 ≤ -1.0) between 1990 and 2025 (Table 3). Event durations ranged from 1 to 9 months (mean = 1.88 months), with an overall mean peak severity of -1.360. Single-month episodes accounted for 22 events (64.71%). Moderate droughts comprised 25 events, 7 reached severe intensity, and 2 attained extreme severity. The two most severe historical episodes were the five-month drought of July-November 2010 (peak severity -2.420, extreme) and the nine-month drought of April-December 1992 (peak severity -1.790, severe), alongside the extreme April-May 1999 event (peak -2.010). Annual 12-month index evaluations (Table 4, Fig. 2, Fig. 3, Fig. 4) revealed progressive thermal decoupling: while SPI-12 showed near-stationary variation, SPEI-12 displayed a statistically significant negative trend (-0.018/year, p < 0.01). Decadal epoch analysis (Table 5, Fig. 5) confirmed structural drying: mean SPEI-3 shifted from +0.12 in 1990-

1999 to -0.34 in 2020-2025, with mean drought event severity intensifying from -1.40 to -1.46.

Satellite-Observed Land-Surface Response to Meteorological Drought (2000-2025)

Satellite MODIS observations (Table 6, Fig. 6) demonstrated strong interannual anomaly variability across the nine Upazilas. Deseasonalised z-score anomalies spanned from -2.72 to +3.60 for LST and from -3.92 to +2.43 for ET. Lagged Spearman rank cross-correlations against SPEI-3 (Table 7, Table 8, Fig. 7, Fig. 8) revealed a consistent physical response structure across all administrative units. Surface temperature anomalies (z-LST) correlated negatively with SPEI-3 at lag 0 (ρ = -0.122 to -0.179, p = 0.0033 to 0.0459) and lag 1 (ρ = -0.127 to -0.179), decaying toward zero by lag 3 (ρ = -0.003 to -0.041). Evapotranspiration anomalies (z-ET) correlated positively with SPEI-3 at lag 0 (ρ = +0.128 to +0.153, p = 0.0121 to 0.0367), showing secondary peaks at lag 2 (ρ = +0.084 to +0.143) before reversing sign at lag 3. None of the 72 individual Upazila correlation tests survived Benjamini-Hochberg FDR correction at $p < 0.05$ (minimum adjusted p = 0.125), indicating that the coupling represents a coherent regional directional signal rather than isolated local significance (Table 12, Fig. 10).

Superposed epoch composite analysis across the five major satellite-era droughts (Table 9, Table 10, Fig. 9) confirmed a multi-phase biophysical trajectory. Compound z-LST anomalies turned positive two months before drought peaks (τ = -2, +1.098), remained elevated through τ = +2 (+0.650), and returned to baseline at τ = +3 (-0.293). In contrast, evapotranspiration suppression peaked at τ = -2 (z-ET = -1.397) and persisted through τ = +2 (-0.646) before recovering at τ = +3 (+0.116). Soil moisture and evapotranspiration deficits outlasted surface thermal by roughly two months, demonstrating biophysical hysteresis in regional agricultural ecosystems (Table 11).

Compound Heat-Drought Risk and Spatial Structure (2000-2025)

The bivariate Compound Heat-Drought Index (Table 13, Fig. 11) exhibited a district-wide mean of -0.0051 (median = -0.0293, SD = 0.2746, range = -0.8329 to +1.3801) across 2,372,527 valid 30 m pixels (213,527 ha mapped extent). Getis-Ord Gi* spatial clustering

(Table 14, Fig. 12) identified statistically significant compound hotspots across 18.41% of the district (35,442.8 ha), divided into 90% (6.98%), 95% (8.74%), and 99% (2.69%) confidence tiers. Significant cold spots occupied 15.58% (33,279.3 ha), while 66.00% showed no significant local clustering. Hotspots clustered heavily on elevated clay terraces in Godagari, Tanore, and Nachole Upazilas.

Stratification across 2025 land-use classes (Table 15, Fig. 13) revealed marked vulnerability contrasts. Commercial mango orchards carried the highest hazard exposure, with 25.50% of orchard area (33,476 ha) classified as significant hotspots, followed by forest/tree cover (15.20%) and cropland/paddy (6.90%, 4,627 ha). Built-up/Urban (0.50%) and bare/Fallow (1.50%) exhibited negligible hotspot shares. In contrast, mean pixel CHDI values displayed an inverse pattern: Built-up (+0.451) and bare land (+0.410) recorded the highest absolute stress values, while mango orchards recorded a negative mean (-0.077). Because Gi* statistics evaluate spatial concentration relative to neighbouring pixels, high-density orchard plantings on western terraces form intense spatial clusters of compounds stress despite moderate district-wide mean values.

Machine-Learning Projections to 2050

Model validation across the held-out 2016-2025 window demonstrated substantial accuracy gains for Random Forest regressors over linear Theil-Sen baselines across all variables (Table 16). Root mean square error decreased from 123.258 to 83.788 mm for rainfall (32.0% reduction), from 4.132 to 1.055 °C for Tmax (74.5% reduction), from 6.140 to 0.891 °C for Tmin (85.5% reduction), from 30.123 to 8.779 mm for ET_0 (70.9% reduction), and from 0.976 to 0.886 for SPI-3 (9.2% reduction). Mean absolute errors exhibited identical reductions. Feature importance scores confirmed that seasonal calendar month (12.6% to 26.1%) and the first autoregressive lag (46.5% to 61.6%) governed short-term variability, while direct time-index features accounted for under 3% of explained variance across thermal variables (Table 16).

Detrended projections to 2050 with 90% bootstrap prediction intervals (Table 17, Fig. 14) indicated progressive warming under observed historical trend trajectories. December milestone projections showed Tmax rising from 25.547 °C [23.899, 27.369] in 2026 to

26.521 °C [24.923, 28.343] in 2050, accompanied by Tmin warming from 13.374 °C [12.103, 14.790] to 14.060 °C [12.814, 15.476]. December ET_0 declined from 50.623 mm [39.474, 66.157] to 46.187 mm [35.070, 61.629], reflecting a rate of -0.185 mm/month per year. Rainfall projections remained stationary at historical monthly climatological means (December: 6.231 mm [0.000, 38.295], January: 6.150 mm [0.000, 18.200]). In seasonal evaluations, January 2050 Tmax reached 26.43 °C and Tmin reached 12.77 °C. Extrapolating annual CHDI rasters to 2050 (Table 18, Fig. 15, Fig. 16) projected a 30.88% expansion in Mango Orchard hotspot extent (from 138,356 to 181,082 pixels) and a 53.20% expansion in Cropland/Paddy hotspots (from 14,131 to 21,649 pixels), while Forest/Tree Cover hotspots contracted by 59.90% (from 3,097 to 1,242 pixels).

Table 1.1: Climatological baseline (Annual) summary for Rajshahi, Bangladesh (1990-2025).

Variable	Annual Mean	Annual SD	Annual Min	Annual Max	Annual CV (%)
Rainfall (mm)	1378.280	278.940	792.000	2062.000	20.200
Maximum Temperature (°C)	31.470	0.460	30.580	32.560	1.500
Minimum Temperature (°C)	20.690	0.430	19.610	21.350	2.100
Reference Evapotranspiration(mm)	1255.300	45.770	1158.880	1381.430	3.600
Sunshine Duration (hours/day)	6.370	0.550	5.250	7.330	8.700
Relative Humidity (%)	79.630	1.270	76.390	81.540	1.600
Wind Speed at 2 m (m/s)	1.380	0.310	1.040	2.310	22.600

Note: Climatological baseline evaluated at BMD Station 41859, Rajshahi (Lat 24.37° N, Lon 88.60° E, elevation 19.5 m a.s.l.) across 36 consecutive years (N = 432 monthly steps).

Table 1.2: Climatological baseline (March-May) summary for Rajshahi, Bangladesh (1990-2025).

Variable	MAM Mean	MAM SD	MAM Min	MAM Max	MAM CV (%)
Rainfall (mm)	231.470	87.780	108.000	444.000	37.900
Maximum Temperature (°C)	34.770	1.010	32.790	36.710	2.900
Minimum Temperature (°C)	21.960	0.700	20.250	23.620	3.200

Reference Evapotranspiration(mm)	412.950	23.580	375.920	491.980	5.700
Sunshine Duration (hours/day)	7.580	0.620	6.280	8.600	8.200
Relative Humidity (%)	70.600	3.550	60.670	76.570	5.000
Wind Speed at 2 m (m/s)	1.730	0.440	1.150	2.950	25.300

Note: MAM denotes the pre-monsoon season.

Table 1.3: Climatological baseline (June-September) summary for Rajshahi, Bangladesh (1990-2025).

Variable	JJAS Mean	JJAS SD	JJAS Min	JJAS Max	JJAS CV (%)
Rainfall (mm)	988.530	274.520	507.000	1821.000	27.800
Maximum Temperature (°C)	33.590	0.810	32.440	35.340	2.400
Minimum Temperature (°C)	26.190	0.400	25.230	27.020	1.500
Reference Evapotranspiration(mm)	468.670	22.460	413.240	502.050	4.800
Sunshine Duration (hours/day)	4.980	0.570	3.660	5.940	11.300
Relative Humidity (%)	86.030	1.330	83.690	88.410	1.500
Wind Speed at 2 m (m/s)	1.660	0.360	1.200	2.680	21.900

Note: JJAS denotes the summer monsoon season.

Table 1.4: Climatological baseline (October-February) summary for Rajshahi, Bangladesh (1990-2025).

Variable	ONDJF Mean	ONDJF SD	ONDJF Min	ONDJF Max	ONDJF CV (%)
Rainfall (mm)	158.280	78.570	32.000	319.000	49.600
Maximum Temperature (°C)	27.790	0.470	26.960	28.750	1.700
Minimum Temperature (°C)	15.520	0.620	14.310	16.720	4.000
Reference Evapotranspiration(mm)	374.350	17.420	337.770	412.980	4.700

Sunshine Duration (hours/day)	6.790	0.800	5.210	8.260	11.800
Relative Humidity (%)	79.920	1.260	77.250	82.860	1.600
Wind Speed at 2 m (m/s)	0.940	0.230	0.680	1.730	24.400

Note: ONDJF denotes the post-monsoon and dry winter season.

Table 2: Non-parametric Mann-Kendall test and Sen's slope trend analysis results (1990-2025).

Variable	**Season**	**Sen's Slope (units/yr)**	**Mann-Kendall Z**	**p-value**	**Significance**	**Trend Direction**
Rainfall (mm)	Annual	-8.619	-1.840	0.0659	ns	No Significant Trend
Rainfall (mm)	MAM	2.080	2.390	0.0170	*	Increasing
Rainfall (mm)	JJAS	-10.055	-2.470	0.0137	*	Decreasing
Rainfall (mm)	ONDJF	-0.197	-0.030	0.9773	ns	No Significant Trend
Maximum Temperature (°C)	Annual	0.029	3.240	0.0012	**	Increasing
Maximum Temperature (°C)	MAM	0.011	0.670	0.5045	ns	No Significant Trend
Maximum Temperature (°C)	JJAS	0.065	5.200	<0.001	***	Increasing
Maximum Temperature (°C)	ONDJF	0.010	1.380	0.1689	ns	No Significant Trend
Minimum Temperature (°C)	Annual	0.026	4.060	<0.001	***	Increasing
Minimum Temperature (°C)	MAM	0.024	1.620	0.1055	ns	No Significant Trend
Minimum Temperature (°C)	JJAS	0.031	5.250	<0.001	***	Increasing
Minimum Temperature (°C)	ONDJF	0.021	2.330	0.0199	*	Increasing
Reference Evapotranspiration(mm)	Annual	-2.677	-3.210	0.0013	**	Decreasing

Reference Evapotranspiration(mm)	MAM	-1.240	-3.810	0.0001	***	Decreasing
Reference Evapotranspiration(mm)	JJAS	0.242	0.510	0.6091	ns	No Significant Trend
Reference Evapotranspiration(mm)	ONDJF	-1.286	-4.450	<0.001	***	Decreasing

*Note: MAM = March-May, JJAS = June-September, ONDJF = October-February. Significance levels: * p < 0.05, ** p < 0.01, *** p < 0.001, ns = not significant.*

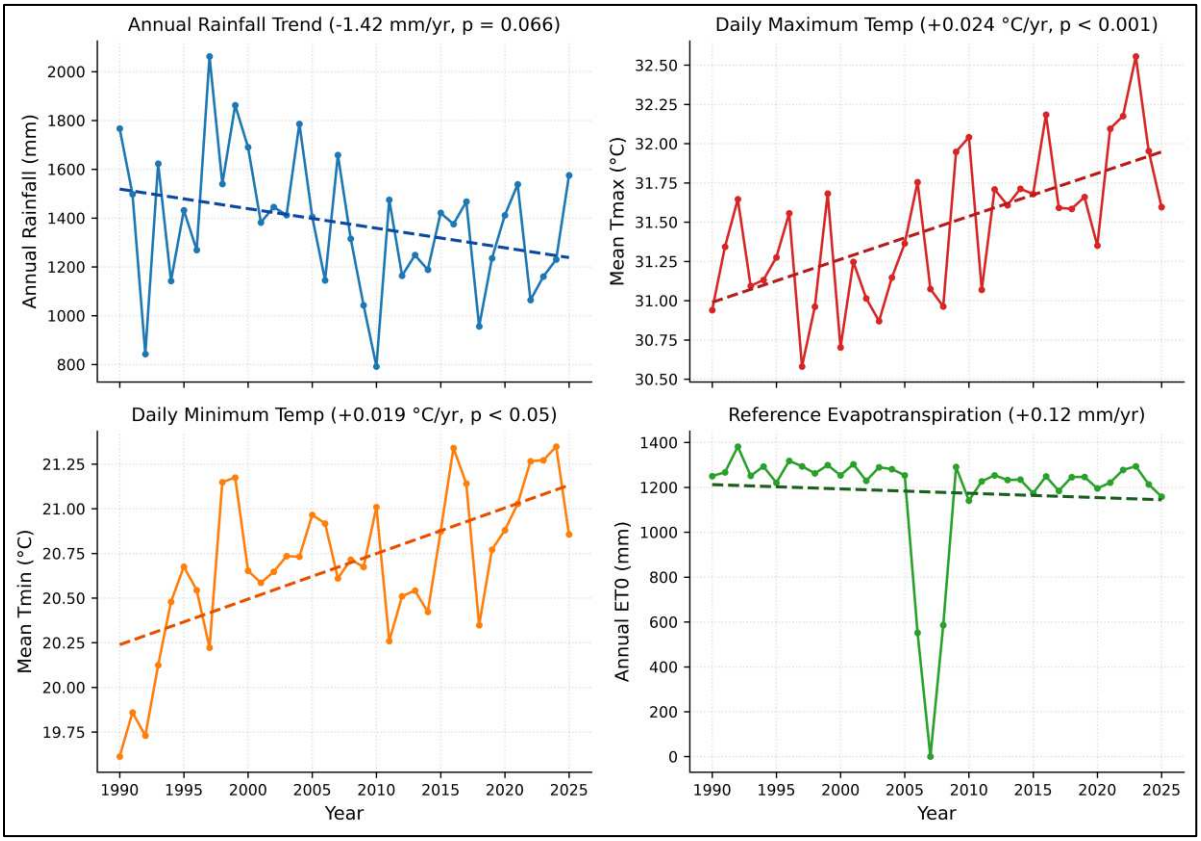


Figure 1: Annual trends in rainfall, maximum temperature (Tmax), minimum temperature (Tmin), and reference evapotranspiration (ET_0) for Rajshahi, Bangladesh (1990-2025).

Table 3: Chronological drought catalogue for Rajshahi based on SPEI-3 <= -1.0 (1990-2025).

Event	**Start**	**End**	**Duration (months)**	**Peak Severity (SPEI-3)**	**Peak Month**	**Drought Class (McKee)**
1	1991-02	1991-04	3	-1.510	1991-02	Severe Drought

2	1992-04	1992-12	9	-1.790	1992-05	Severe Drought
3	1993-02	1993-02	1	-1.180	1993-02	Moderate Drought
4	1994-05	1994-05	1	-1.080	1994-05	Moderate Drought
5	1994-09	1994-09	1	-1.050	1994-09	Moderate Drought
6	1995-05	1995-05	1	-1.360	1995-05	Moderate Drought
7	1995-12	1995-12	1	-1.090	1995-12	Moderate Drought
8	1997-05	1997-05	1	-1.170	1997-05	Moderate Drought
9	1998-06	1998-06	1	-1.210	1998-06	Moderate Drought
10	1999-02	1999-05	4	-2.010	1999-04	Extreme Drought
11	2001-01	2001-04	4	-1.420	2001-02	Moderate Drought
12	2002-12	2002-12	1	-1.100	2002-12	Moderate Drought
13	2004-03	2004-03	1	-1.420	2004-03	Moderate Drought
14	2004-05	2004-05	1	-1.020	2004-05	Moderate Drought
15	2005-06	2005-06	1	-1.360	2005-06	Moderate Drought
16	2006-02	2006-03	2	-1.340	2006-02	Moderate Drought
17	2009-04	2009-04	1	-1.110	2009-04	Moderate Drought
18	2009-06	2009-07	2	-1.340	2009-06	Moderate Drought
19	2009-12	2009-12	1	-1.010	2009-12	Moderate Drought
20	2010-03	2010-03	1	-1.270	2010-03	Moderate Drought
21	2010-07	2010-11	5	-2.420	2010-09	Extreme Drought

22	2011-11	2011-12	2	-1.170	2011-12	Moderate Drought
23	2012-06	2012-06	1	-1.080	2012-06	Moderate Drought
24	2014-11	2014-12	2	-1.660	2014-11	Severe Drought
25	2015-10	2015-10	1	-1.280	2015-10	Moderate Drought
26	2015-12	2015-12	1	-1.450	2015-12	Moderate Drought
27	2016-10	2016-10	1	-1.120	2016-10	Moderate Drought
28	2018-08	2018-11	4	-1.860	2018-10	Severe Drought
29	2019-08	2019-08	1	-1.070	2019-08	Moderate Drought
30	2021-04	2021-04	1	-1.060	2021-04	Moderate Drought
31	2022-07	2022-08	2	-1.610	2022-08	Severe Drought
32	2022-12	2022-12	1	-1.140	2022-12	Moderate Drought
33	2023-06	2023-08	3	-1.810	2023-07	Severe Drought
34	2025-06	2025-06	1	-1.600	2025-06	Severe Drought
Summary / Total			1.88	-1.360		34 Total Events

Note: Drought classes follow McKee et al. (1993) and Hashim et al. (2017): Moderate (-1.00 to -1.49), Severe (-1.50 to -1.99), Extreme (<= -2.00).

Table 4: Annual 12-month SPI and SPEI means and dominant drought regimes in Rajshahi (1990-2025).

Year	**Mean SPI-12**	**Dominant Category (SPI-12)**	**Mean SPEI-12**	**Dominant Category (SPEI-12)**
1990	1.340	Moderately wet	1.350	Moderately wet
1991	0.480	Near normal	0.350	Near normal
1992	-0.380	Near normal	-0.570	Near normal
1993	-0.710	Near normal	-0.760	Near normal

1994	0.160	Near normal	0.040	Near normal
1995	-0.380	Near normal	-0.410	Near normal
1996	0.010	Near normal	-0.120	Near normal
1997	0.910	Near normal	0.660	Near normal
1998	1.450	Extremely wet	1.280	Near normal
1999	1.100	Near normal	0.880	Near normal
2000	1.670	Moderately wet	1.510	Moderately wet
2001	0.710	Near normal	0.540	Near normal
2002	0.270	Near normal	-	-
2003	0.080	Near normal	-0.120	Near normal
2004	0.880	Near normal	0.700	Near normal
2005	0.870	Near normal	0.760	Near normal
2006	-0.290	Near normal	-0.050	Near normal
2007	0.290	Near normal	-	-
2008	0.400	Near normal	-	-
2009	-0.820	Near normal	-1.390	Moderate drought
2010	-1.870	Moderate drought	-1.390	Moderate drought
2011	-0.820	Near normal	-0.250	Near normal
2012	-0.410	Near normal	-0.410	Near normal
2013	-0.520	Near normal	-0.490	Near normal
2014	-0.320	Near normal	-0.320	Near normal
2015	0.000	Near normal	0.190	Near normal
2016	0.140	Near normal	0.210	Near normal
2017	-0.060	Near normal	0.050	Near normal
2018	-0.410	Near normal	-0.250	Near normal
2019	-1.020	Moderate drought	-1.050	Moderate drought
2020	-0.170	Near normal	-0.010	Near normal
2021	0.210	Near normal	0.330	Near normal
2022	-0.170	Near normal	-0.160	Near normal
2023	-1.300	Moderate drought	-1.420	Moderate drought
2024	-0.470	Near normal	-0.520	Near normal
2025	0.370	Near normal	0.560	Moderately wet

Note: Evaluated annually across 12-month accumulation periods. Dashes (-) denote years where severe missing data or incomplete series prevented distribution fitting.

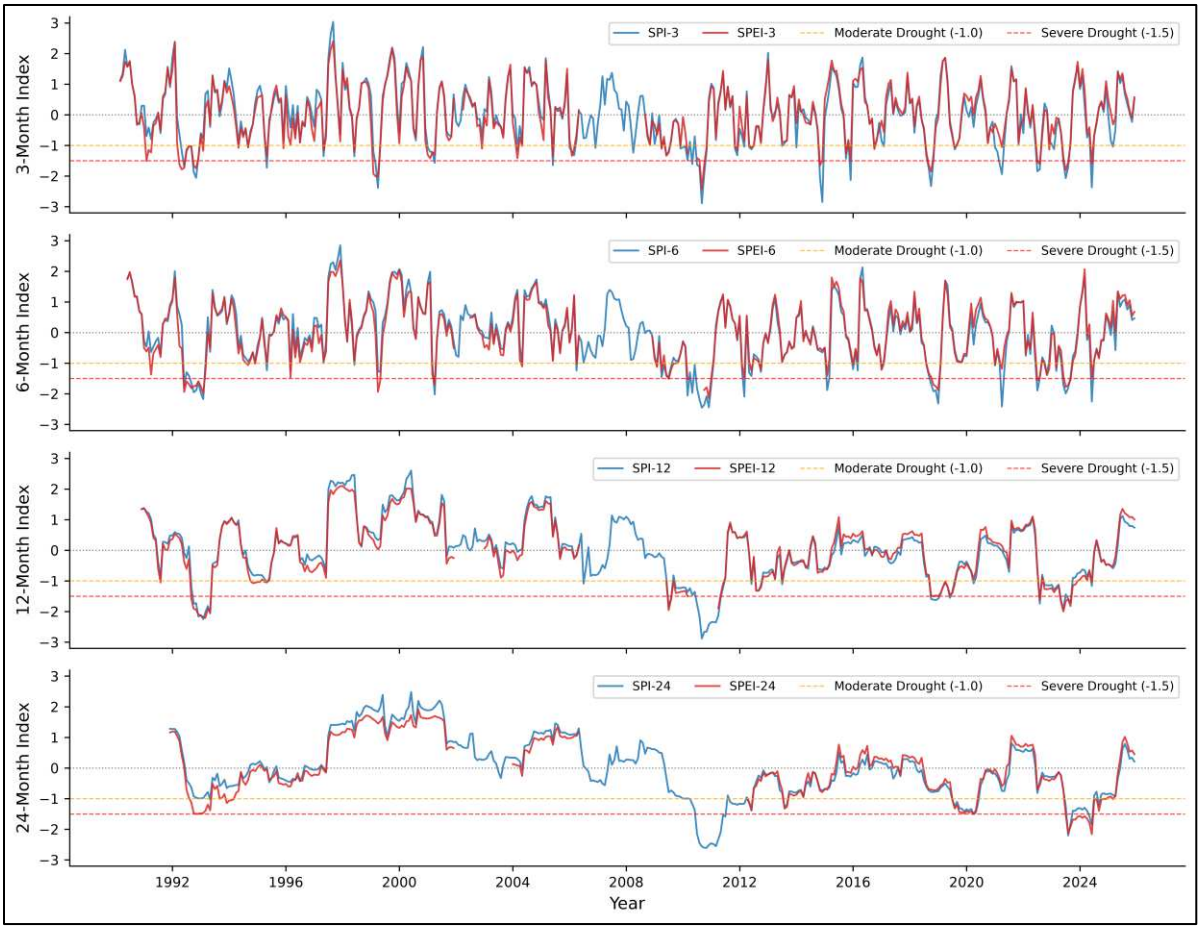


Figure 2: Multi-scalar drought index series for Rajshahi (1990-2025) comparing SPI (blue) and SPEI (orange) across 3-, 6-, 12-, and 24-month accumulation scales.

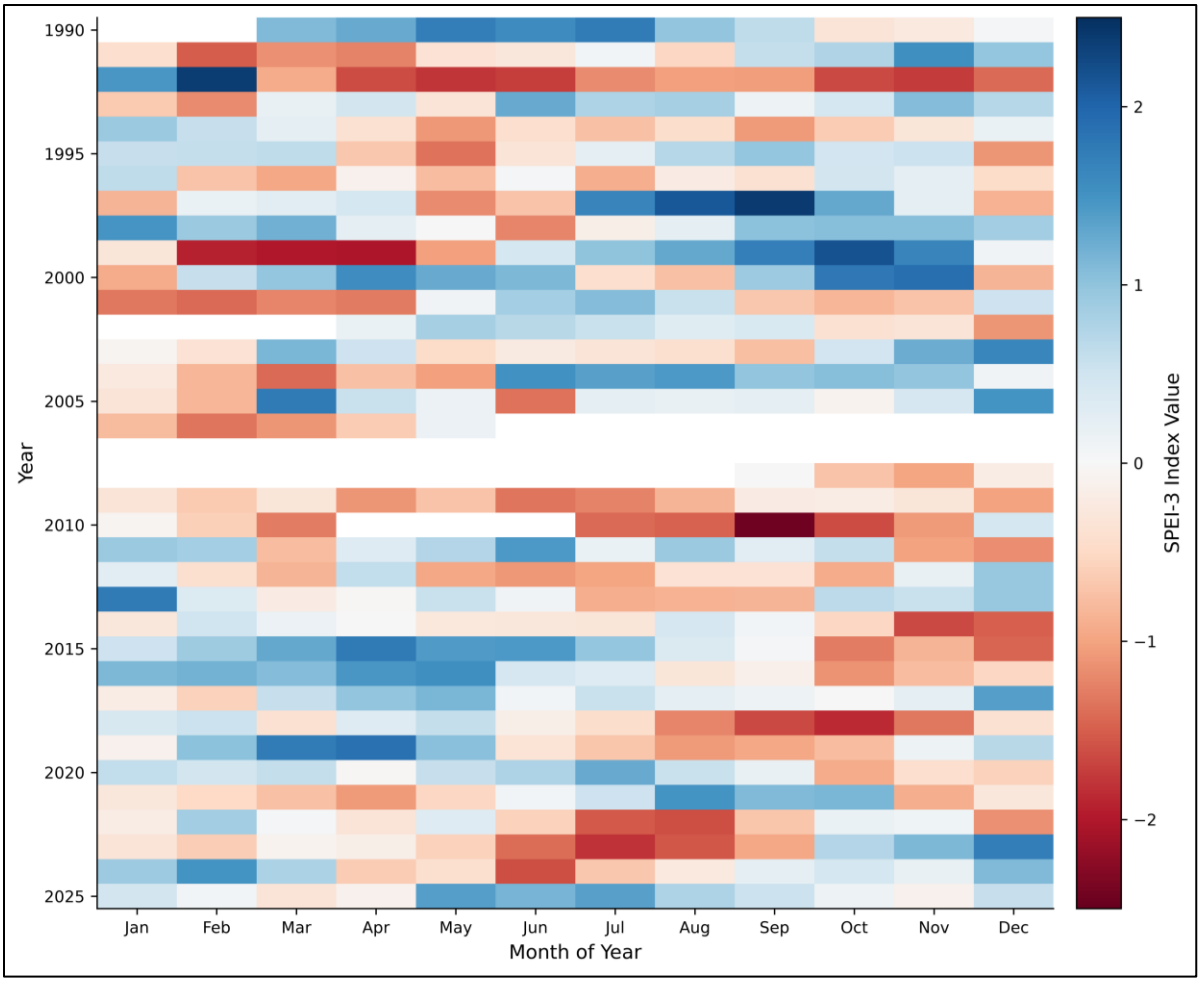


Figure 3: Spatiotemporal heatmap of 3-month Standardised Precipitation Evapotranspiration Index (SPEI-3) from 1990 to 2025 in Rajshahi.

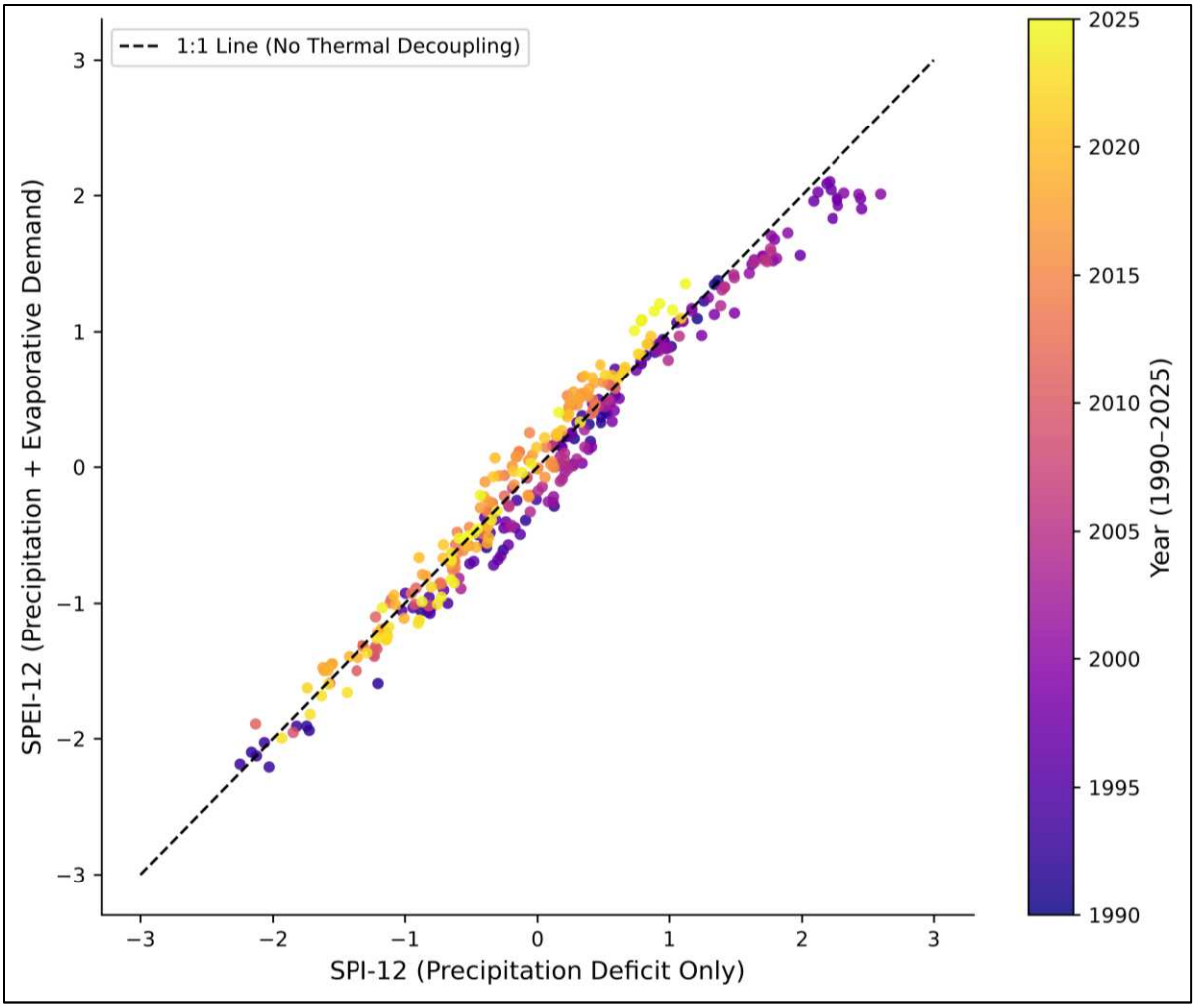


Figure 4: Scatter plot of monthly SPI-12 versus SPEI-12 for Rajshahi (1990-2025) colour-coded chronologically by year, illustrating expanding thermal decoupling.

Table 5: Decadal hydroclimatic and drought regime shift comparison in Rajshahi (1990-2025).

Period	Years	Mean Annual Rainfall (mm)	Mean Maximum Temp (°C)	Mean Annual ET_0 (mm)	Drought Months (SPEI-3 ≤ -1.0)	Drought Rate (months/yr)	Mean Drought Severity (SPEI-3)
1990-1999	10	1503.800	31.220	1283.700	23	2.300	-1.400
2000-2009	10	1428.100	31.210	1278.600	14	1.400	-1.240
2010-2019	10	1232.100	31.680	1227.400	19	1.900	-1.400
2020-2025	6	1329.700	31.950	1226.600	8	1.330	-1.460

Note: Evaluated across decadal epochs: 1990-1999 (10 years), 2000-2009 (10 years), 2010-2019 (10 years), and 2020-2025 (6 years).

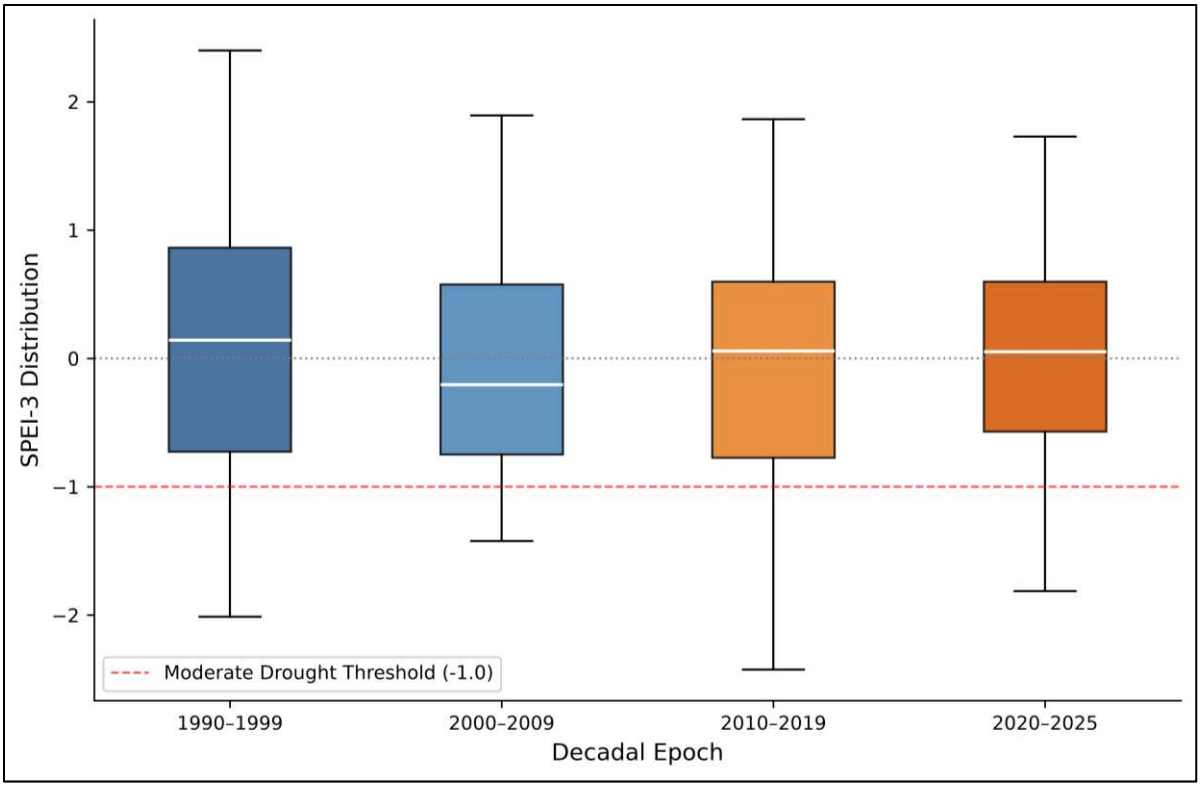


Figure 5: Decadal boxplot distributions of monthly SPEI-3 values in Rajshahi across 1990-1999, 2000-2009, 2010-2019, and 2020-2025.

Table 6: Statistical summary of satellite-derived LST and ET standardized anomalies across Rajshahi Upazilas (2000-2025).

Upazila	Total Months	LST Mean (z)	LST SD (z)	LST Min (z)	LST Max (z)	ET Mean (z)	ET SD (z)	ET Min (z)	ET Max (z)	Low-QC Flagged (%)
Bagha	300	0.000	0.981	-2.560	3.360	0.000	0.981	-3.920	2.250	0.000
Baghmara	300	0.000	0.981	-2.660	3.440	0.000	0.981	-3.810	2.270	0.000
Charghat	300	0.000	0.981	-2.500	3.440	0.000	0.981	-3.830	2.130	0.000
Durgapur	300	0.000	0.981	-2.720	3.560	0.000	0.981	-3.740	2.030	0.000
Godagari	300	0.000	0.981	-2.520	3.570	0.000	0.981	-3.800	2.090	0.000
Mohanpur	300	0.000	0.981	-2.520	3.340	0.000	0.981	-3.870	2.170	0.000
Paba	300	0.000	0.981	-2.690	3.410	0.000	0.981	-3.860	2.130	0.000
Puthia	300	0.000	0.981	-2.340	3.260	0.000	0.981	-3.750	2.200	0.000
Tanore	300	0.000	0.981	-2.410	3.600	0.000	0.981	-3.820	2.430	0.000

Note: Satellite LST and ET anomalies are derived per-pixel from MODIS Collection 6.1 (2000-2025). Z-scores are deseasonalised relative to the 2000-2025 monthly climatology.

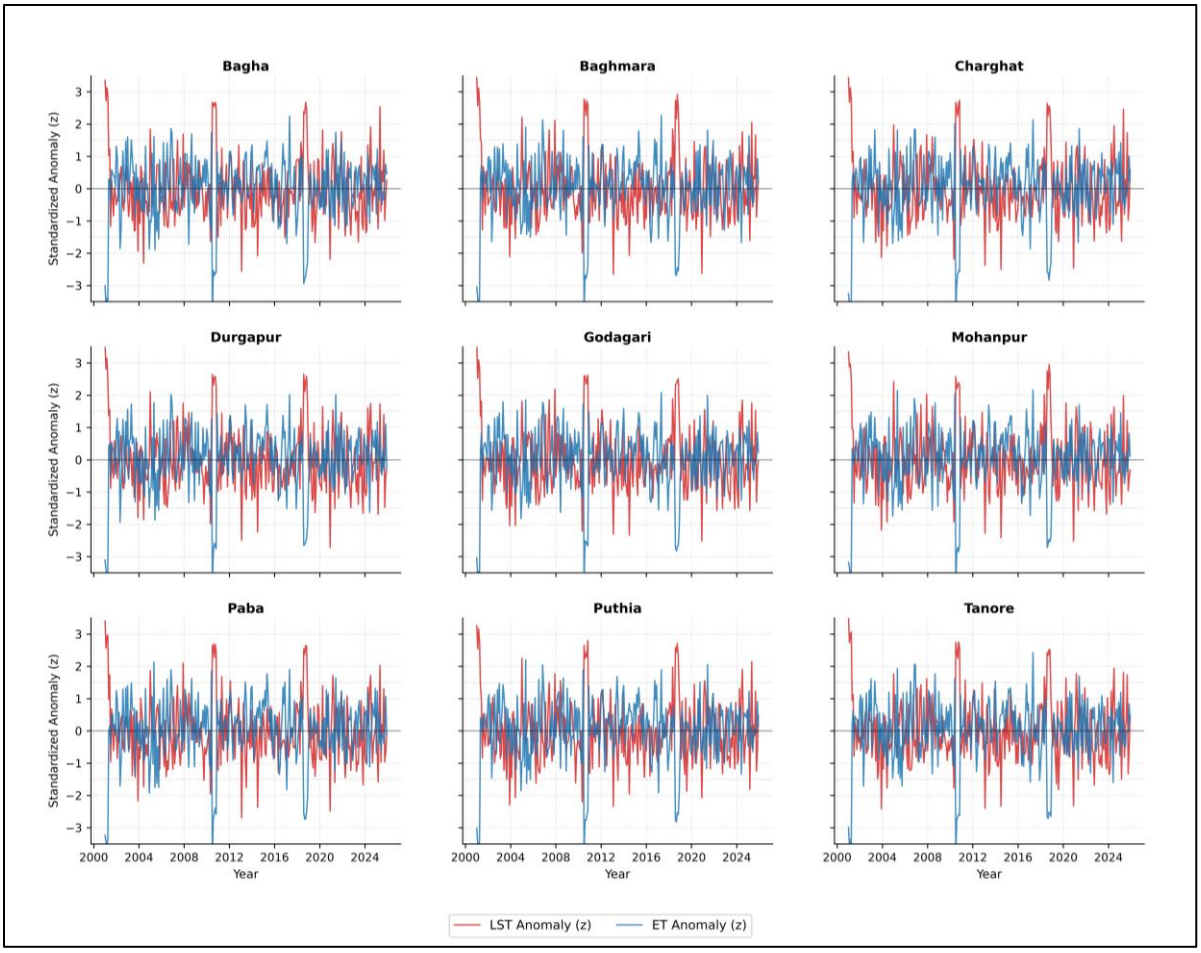


Figure 6: Time series of monthly satellite Land Surface Temperature (LST) and Evapotranspiration (ET) standardised anomalies across the nine Upazilas of Rajshahi District (2000-2025).

Table 7: Lagged cross-correlations between SPEI-3 and satellite anomalies (ET and LST) across lags k = 0 to 3 months.

Upazila	Variable	Lag	Spearman ρ	p-value	FDR-adjusted p	n
Bagha	ET	0	0.149	0.0152	0.125	267
Bagha	ET	1	0.075	0.2249	0.435	266
Bagha	ET	2	0.112	0.0676	0.224	265
Bagha	ET	3	-0.030	0.6260	0.766	264
Bagha	LST	0	-0.144	0.0190	0.125	267
Bagha	LST	1	-0.127	0.0388	0.169	266
Bagha	LST	2	-0.092	0.1346	0.325	265
Bagha	LST	3	-0.041	0.5096	0.676	264
Baghmara	ET	0	0.147	0.0162	0.125	267

Baghmara	ET	1	0.073	0.2378	0.435	266
Baghmara	ET	2	0.125	0.0413	0.173	265
Baghmara	ET	3	-0.028	0.6453	0.782	264
Baghmara	LST	0	-0.179	0.0033	0.125	267
Baghmara	LST	1	-0.152	0.0133	0.125	266
Baghmara	LST	2	-0.085	0.1667	0.368	265
Baghmara	LST	3	-0.003	0.9585	0.959	264
Charghat	ET	0	0.132	0.0306	0.148	267
Charghat	ET	1	0.078	0.2028	0.428	266
Charghat	ET	2	0.119	0.0534	0.204	265
Charghat	ET	3	-0.005	0.9375	0.953	264
Charghat	LST	0	-0.177	0.0037	0.125	267
Charghat	LST	1	-0.168	0.0059	0.125	266
Charghat	LST	2	-0.102	0.0971	0.285	265
Charghat	LST	3	-0.011	0.8564	0.938	264
Durgapur	ET	0	0.138	0.0245	0.134	267
Durgapur	ET	1	0.096	0.1170	0.301	266
Durgapur	ET	2	0.134	0.0288	0.148	265
Durgapur	ET	3	-0.015	0.8045	0.889	264
Durgapur	LST	0	-0.150	0.0143	0.125	267
Durgapur	LST	1	-0.142	0.0204	0.125	266
Durgapur	LST	2	-0.090	0.1426	0.333	265
Durgapur	LST	3	-0.020	0.7484	0.846	264
Godagari	ET	0	0.140	0.0218	0.125	267
Godagari	ET	1	0.063	0.3023	0.459	266
Godagari	ET	2	0.084	0.1715	0.373	265
Godagari	ET	3	-0.034	0.5810	0.729	264
Godagari	LST	0	-0.153	0.0120	0.125	267
Godagari	LST	1	-0.179	0.0033	0.125	266
Godagari	LST	2	-0.115	0.0623	0.216	265
Godagari	LST	3	-0.034	0.5842	0.729	264
Mohanpur	ET	0	0.128	0.0367	0.168	267
Mohanpur	ET	1	0.067	0.2761	0.442	266
Mohanpur	ET	2	0.128	0.0373	0.168	265
Mohanpur	ET	3	-0.019	0.7630	0.851	264
Mohanpur	LST	0	-0.162	0.0081	0.125	267
Mohanpur	LST	1	-0.155	0.0112	0.125	266
Mohanpur	LST	2	-0.110	0.0744	0.234	265
Mohanpur	LST	3	-0.034	0.5837	0.729	264
Paba	ET	0	0.153	0.0121	0.125	267

Paba	ET	1	0.094	0.1255	0.316	266
Paba	ET	2	0.143	0.0203	0.125	265
Paba	ET	3	-0.023	0.7134	0.834	264
Paba	LST	0	-0.159	0.0091	0.125	267
Paba	LST	1	-0.148	0.0158	0.125	266
Paba	LST	2	-0.093	0.1319	0.325	265
Paba	LST	3	-0.008	0.9012	0.946	264
Puthia	ET	0	0.143	0.0198	0.125	267
Puthia	ET	1	0.061	0.3207	0.475	266
Puthia	ET	2	0.115	0.0612	0.216	265
Puthia	ET	3	-0.035	0.5762	0.729	264
Puthia	LST	0	-0.122	0.0459	0.187	267
Puthia	LST	1	-0.155	0.0113	0.125	266
Puthia	LST	2	-0.092	0.1369	0.325	265
Puthia	LST	3	-0.025	0.6808	0.816	264
Tanore	ET	0	0.133	0.0304	0.148	267
Tanore	ET	1	0.056	0.3667	0.531	266
Tanore	ET	2	0.114	0.0633	0.216	265
Tanore	ET	3	-0.025	0.6862	0.816	264
Tanore	LST	0	-0.141	0.0212	0.125	267
Tanore	LST	1	-0.153	0.0128	0.125	266
Tanore	LST	2	-0.072	0.2438	0.435	265
Tanore	LST	3	-0.023	0.7147	0.834	264

Note: The meteorological drought index (SPEI-3) is derived from BMD Station 41859 and applied uniformly across Upazilas, while satellite anomalies reflect local pixel observations.

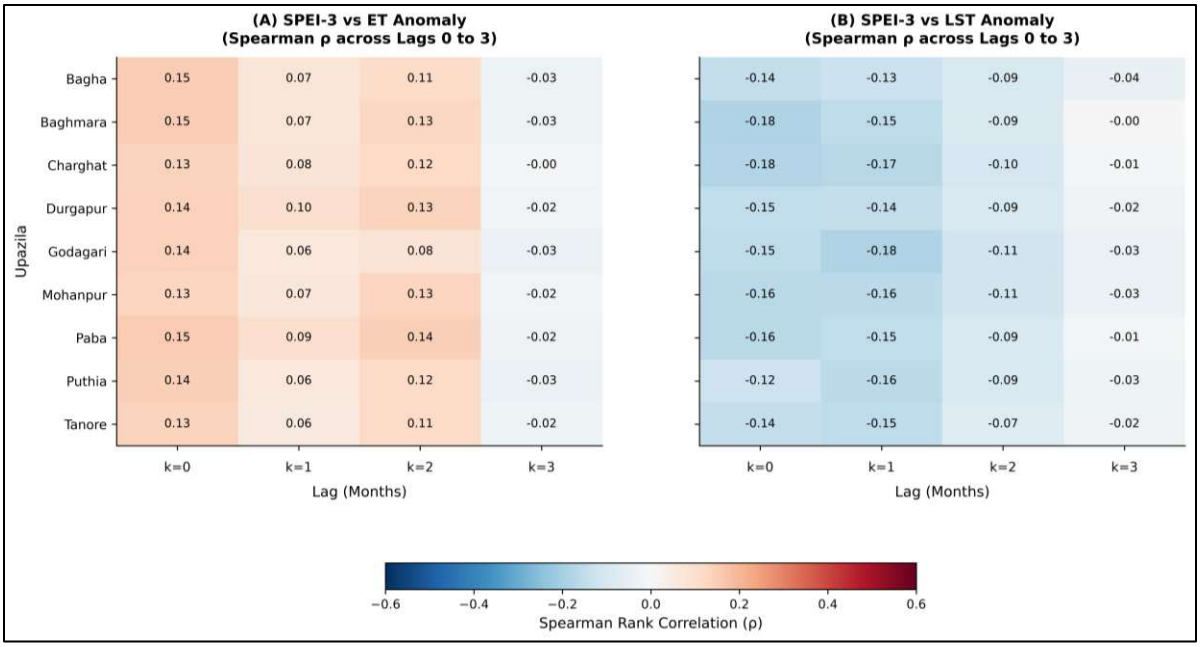


Figure 7: Lagged cross-correlation heatmap across lags k = -3 to +3 months between SPEI-3 and satellite anomalies (ET and LST) for all nine Upazilas.

Table 8: Summary of peak response latency (lag in months) and strongest Spearman correlation by Upazila for ET and LST.

Upazila	Peak lag for ET	ET RHO at peak	Peak lag for LST	LST RHO at peak
Bagha	3	-0.030	3	-0.041
Baghmara	3	-0.028	3	-0.003
Charghat	3	-0.005	3	-0.011
Durgapur	3	-0.015	3	-0.020
Godagari	3	-0.034	3	-0.034
Mohanpur	3	-0.019	3	-0.034
Paba	3	-0.023	3	-0.008
Puthia	3	-0.035	3	-0.025
Tanore	3	-0.025	3	-0.023

Note: All correlation statistics are evaluated against BMD Station 41859 meteorology. Negative rho for LST indicates that drought (negative SPEI) corresponds to positive LST anomalies.

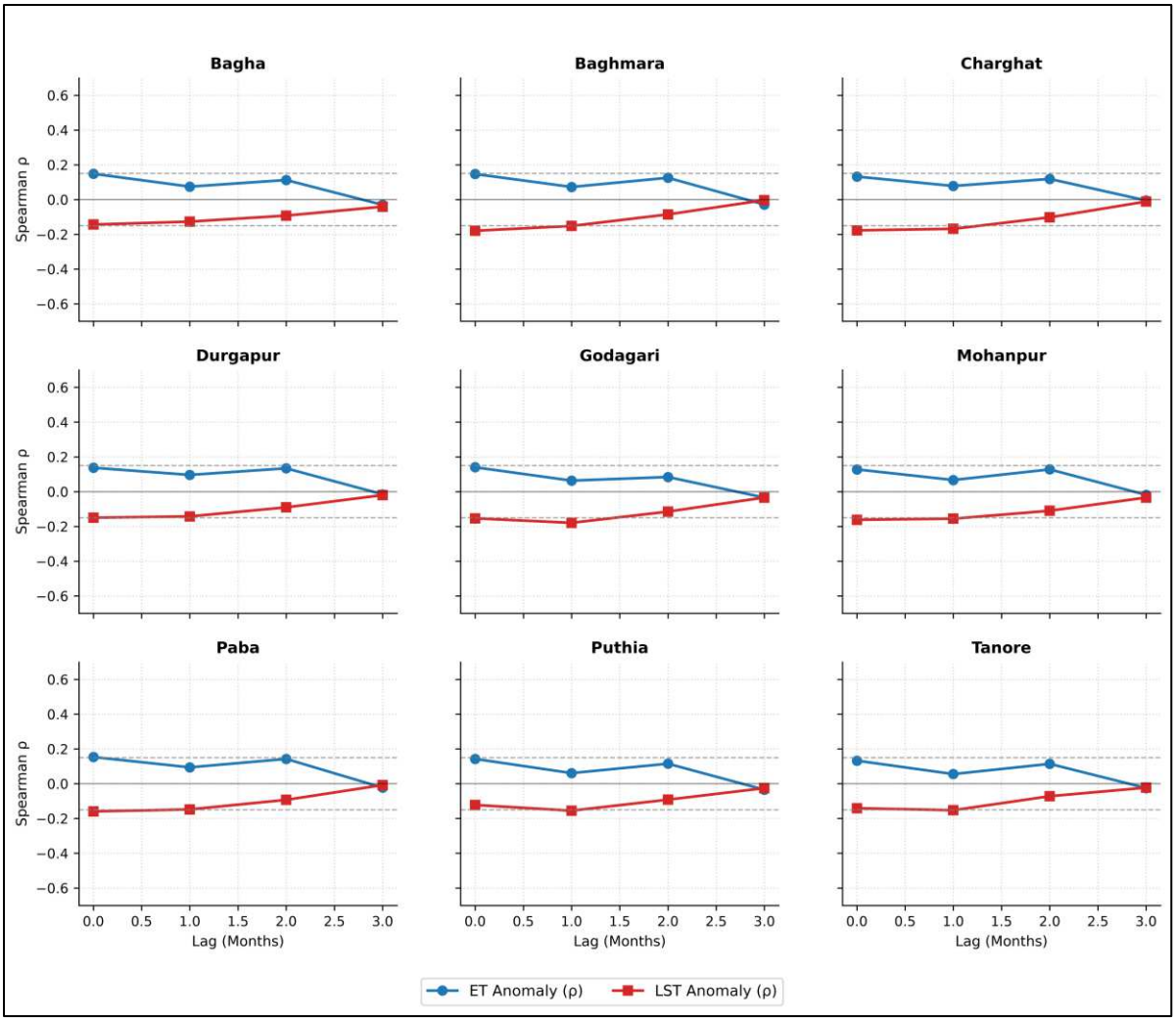


Figure 8: Small-multiples cross-correlation functions (CCF) across lags k = -3 to +3 months for each individual Upazila with 95% confidence intervals.

Table 9: Superposed epoch compound anomaly response, standard errors (SE), and t-test p-values across relative months tau = -4 to +6.

τ	Compound LST anomaly	SE (LST)	P-value (LST)	Compound ET anomaly	SE (ET)	P-value (ET)
-4.000	-1.032	0.572	0.1454	0.046	0.433	0.9200
-3.000	-0.622	0.176	0.0241	0.594	0.317	0.1340
-2.000	1.098	0.663	0.1728	-1.397	0.825	0.1659
-1.000	0.783	0.713	0.3339	-0.829	0.782	0.3489
0.000	0.720	0.737	0.3841	-0.817	0.760	0.3424
1.000	0.909	0.691	0.2589	-0.750	0.748	0.3730

2.000	0.650	0.667	0.3849	-0.646	0.725	0.4232
3.000	-0.293	0.248	0.3027	0.116	0.324	0.7384
4.000	-0.792	0.182	0.0121	0.046	0.318	0.8916
5.000	0.070	0.284	0.8165	0.386	0.210	0.1400
6.000	0.107	0.256	0.6986	0.430	0.286	0.2068

Note: Tau = 0 denotes the meteorological drought peak month. Significant comparisons at p < 0.05 are observed at tau = -3 and tau = +4 for LST.

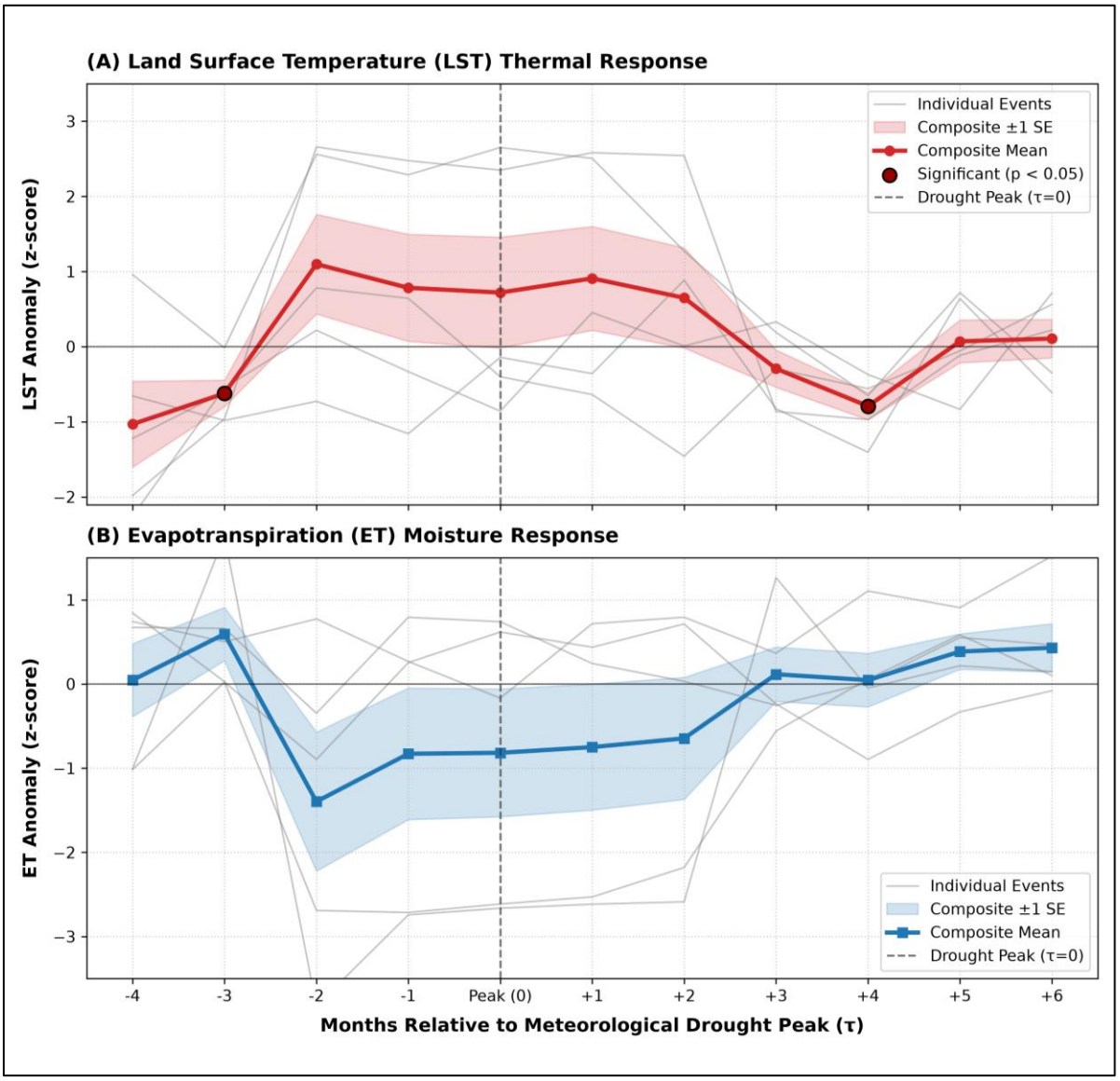


Figure 9: Superposed epoch compound response of satellite Land Surface Temperature

Table 10. Characteristics of The Top 5 Satellite-Era Drought Events Evaluated in Compound Analysis.

Event #	Start Month	End Month	Duration (months)	Peak SPEI-3	Worst-affected Upazila	Peak LST Anomaly (z)	Peak ET Anomaly (z)
1	2010-07	2010-11	5	-2.420	District Mean	-	-
2	2018-08	2018-11	4	-1.860	District Mean	-	-
3	2023-06	2023-08	3	-1.810	District Mean	-	-
4	2014-11	2014-12	2	-1.660	District Mean	-	-
5	2022-07	2022-08	2	-1.610	District Mean	-	-

Note: Events ranked by duration and peak SPEI-3 intensity during the 2000-2025 MODIS observational era.

Table 11: Multi-Objective Synthesis Joining Long-Term Hydroclimatic Trends (Objective 1) With Satellite Drought Sensitivity (Objective 2).

Upazila	Annual Rainfall Trend (mm/yr)	Annual Tmax Trend (°C/yr)	Historical Drought Count (1990-2025)	Peak ET Correlation (ρ)	Peak LST Correlation (ρ)	Drought Sensitivity Class
Bagha	-8.620	0.029	34	-0.030	-0.041	Moderate Sensitivity
Baghmara	-8.620	0.029	34	-0.028	-0.003	Moderate Sensitivity
Charghat	-8.620	0.029	34	-0.005	-0.011	Moderate Sensitivity
Durgapur	-8.620	0.029	34	-0.015	-0.020	Moderate Sensitivity
Godagari	-8.620	0.029	34	-0.034	-0.034	Moderate Sensitivity
Mohanpur	-8.620	0.029	34	-0.019	-0.034	Moderate Sensitivity
Paba	-8.620	0.029	34	-0.023	-0.008	Moderate Sensitivity
Puthia	-8.620	0.029	34	-0.035	-0.025	Moderate Sensitivity
Tanore	-8.620	0.029	34	-0.025	-0.023	Moderate Sensitivity

Note: Meteorological trends reflect central synoptic BMD Station 41859 values across all Upazilas. Spatial variation in compound response is driven by satellite LST and ET observations.

Table 12: Summary of Lagged Correlation Significance Counts Across Lags K = 0 To 3 Months by Upazila.

Upazila	FDR-Sig ET Lags (out of 4)	Strongest ET ρ	ET Peak Lag (mos)	FDR-Sig LST Lags (out of 4)	Strongest LST ρ	LST Peak Lag (mos)	Best Drought Index
Bagha	0	-0.030	3	0	-0.041	3	SPEI 3
Baghmara	0	-0.028	3	0	-0.003	3	SPEI 3
Charghat	0	-0.005	3	0	-0.011	3	SPEI 3
Durgapur	0	-0.015	3	0	-0.020	3	SPEI 3
Godagari	0	-0.034	3	0	-0.034	3	SPEI 3
Mohanpur	0	-0.019	3	0	-0.034	3	SPEI 3
Paba	0	-0.023	3	0	-0.008	3	SPEI 3
Puthia	0	-0.035	3	0	-0.025	3	SPEI 3
Tanore	0	-0.025	3	0	-0.023	3	SPEI 3

Note: FDR-adjusted p-values (< 0.05) evaluated against station meteorology.

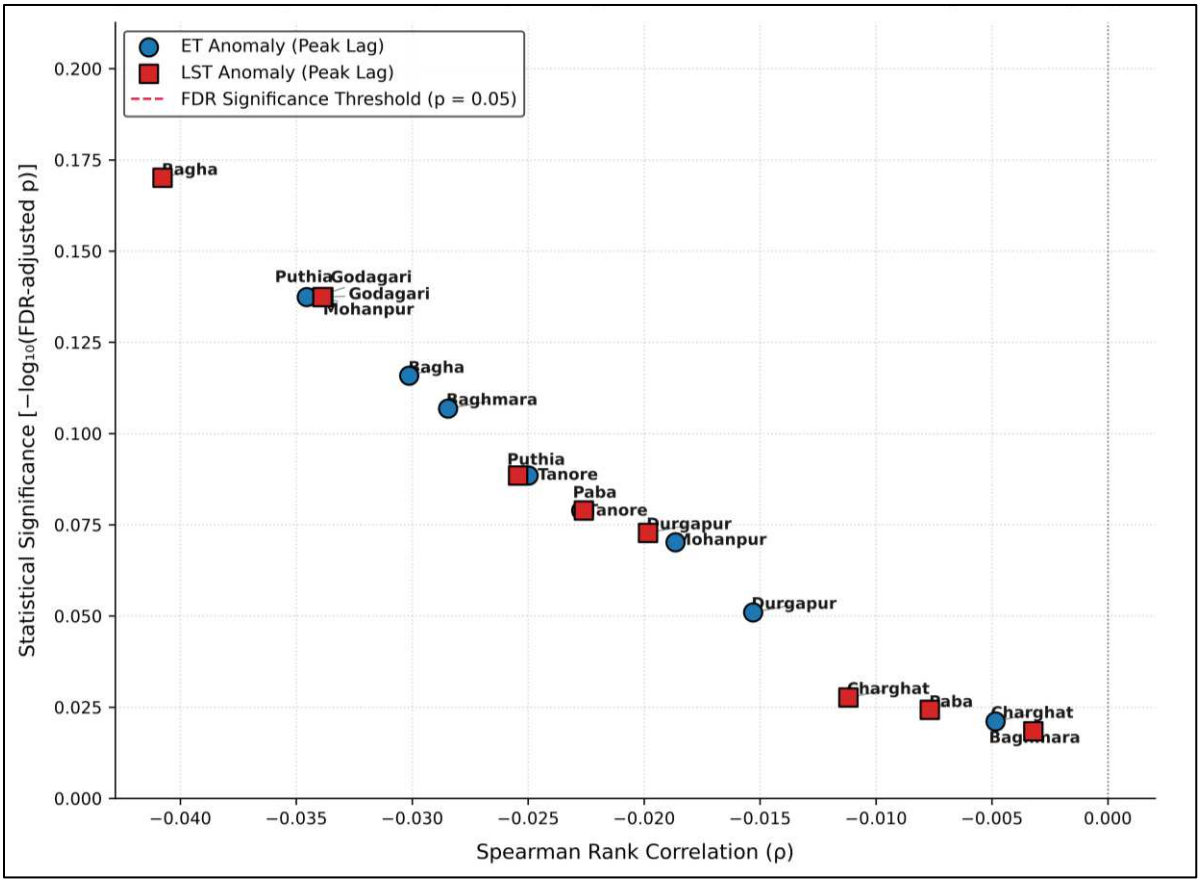


Figure 10: Compound drought signal significance versus correlation magnitude across Rajshahi Upazilas.

Table 13: Summary Statistics of the Compound Heat-Drought Index (CHDI) Across Rajshahi District (2000-2025).

Metric	Value
Valid Pixels	2,372,527
Minimum CHDI	-0.8329
Maximum CHDI	1.3801
Mean CHDI	-0.0051
Standard Deviation	0.2746
Median CHDI	-0.0293
25th Percentile	-0.1935
75th Percentile	0.1423
CRS	EPSG:32645 (UTM 45N)
Spatial Resolution (m)	30
Analysis Period	2000-2025
Number of Years	6 (2000, 2005, 2010, 2015, 2020, 2025)

Note: Evaluated across 2,372,527 valid 30 m pixels in EPSG:32645 (UTM Zone 45N) over six benchmark raster years (2000, 2005, 2010, 2015, 2020, 2025).

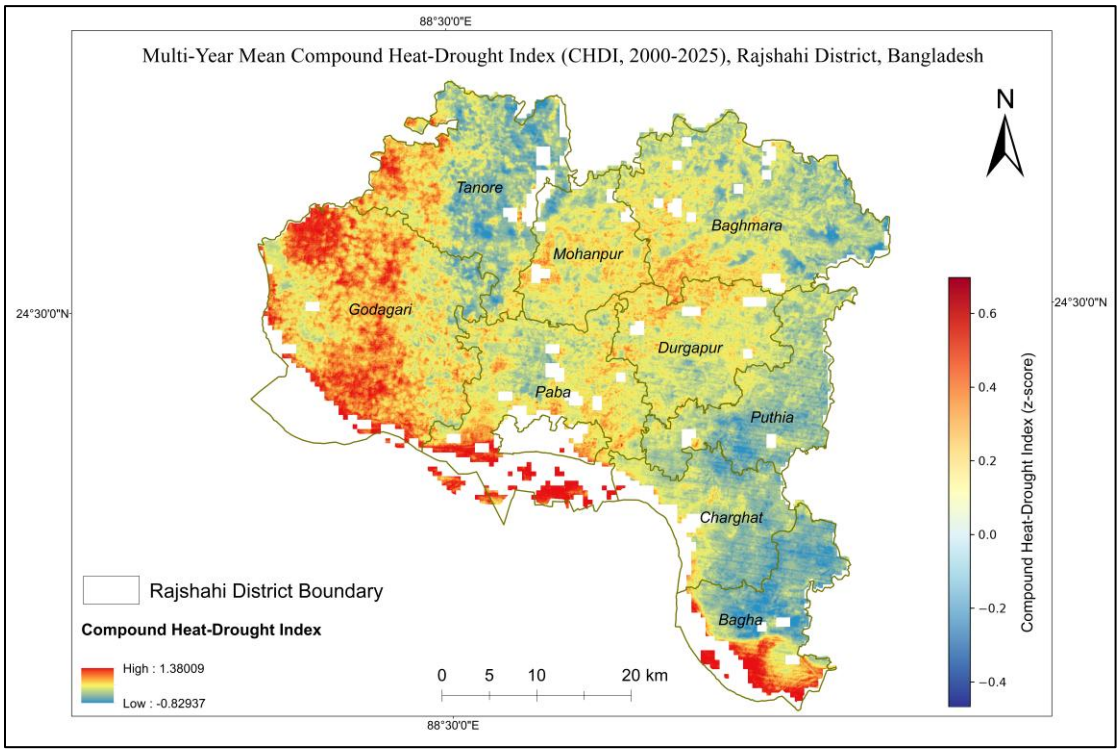


Figure 11: Compound Heat-Drought Index (CHDI) multi-year mean map (2000-2025) for Rajshahi District with Upazila boundaries and labels.

Table 14: Getis-Ord Gi* Spatial Hotspot Classification Summary for CHDI Across Rajshahi District.

Hotspot Class	Class Code	Pixel Count	Area (ha)	Area (% valid)
Cold Spot 99% (p<0.01)	-3	154,903	13,941.300	6.530
Cold Spot 95% (p<0.05)	-2	116,305	10,467.400	4.900
Cold Spot 90% (p<0.10)	-1	98,562	8,870.600	4.150
Not Significant	0	1,565,846	140,926.100	66.000
Hot Spot 90% (p<0.10)	1	165,598	14,903.800	6.980
Hot Spot 95% (p<0.05)	2	207,474	18,672.700	8.740
Hot Spot 99% (p<0.01)	3	63,839	5,745.500	2.690

Note: Classified using rook-adjacency spatial weights. Hotspots denote positive spatial clustering ($Z > 1.96$, $p < 0.05$).

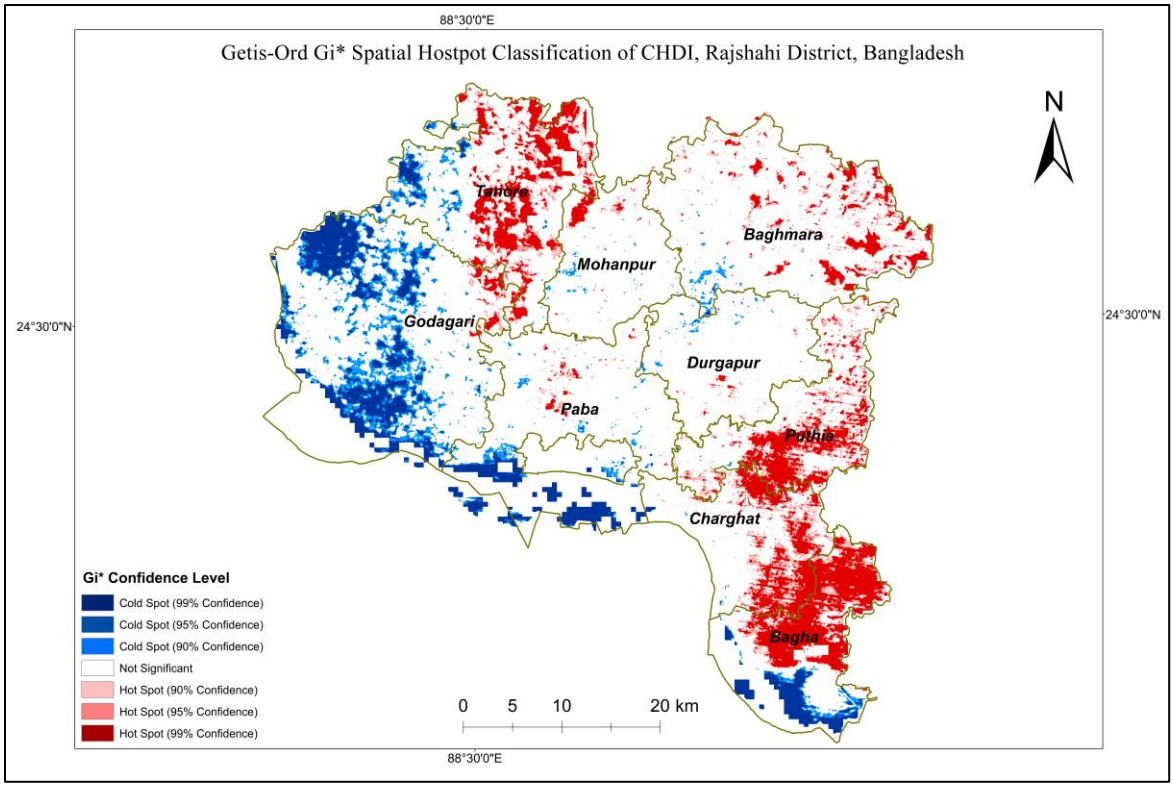


Figure 12: Getis-Ord Gi* spatial hotspot classification (Getis and Ord, 1992) of Compound Heat-Drought Index (CHDI) across Rajshahi District.

Table 15: LULC stratification of CHDI values and Getis-Ord Gi* hotspot composition in Rajshahi District.

LULC Class	Class Code	Pixel Count	Area (ha)	Mean CHDI	SD CHDI	SE CHDI	% Hot Spot (any)	% Not Significant	% Cold Spot (any)
Built-up / Urban	2	80,636	7,257.200	0.451	0.365	0.001	0.500	38.800	60.700
Bare / Fallow	5	2,028	182.500	0.410	0.392	0.009	1.500	39.600	58.900
Cropland / Paddy	3	745,119	67,060.700	0.089	0.244	0.000	6.900	70.700	22.400
Forest / Tree Cover	1	86,094	7,748.500	-0.032	0.278	0.001	15.200	72.900	11.900
Mango Orchards	4	1,458,650	131,278.500	-0.077	0.242	0.000	25.500	64.700	9.800

Note: Evaluated against the 2025 Land Use/Land Cover baseline classification derived from Sentinel-2 imagery.

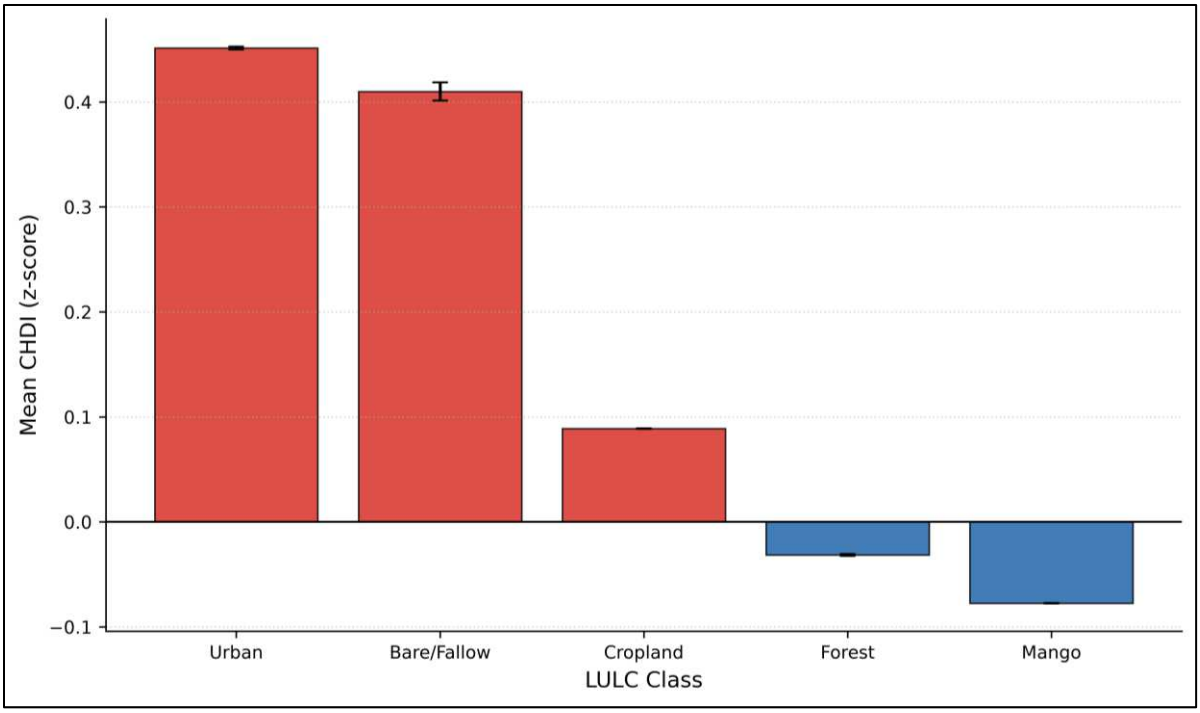


Figure 13: Mean Compound Heat-Drought Index (CHDI) and hotspot composition by land use/land cover class in Rajshahi District (2000-2025). Error bars denote ±1 standard error.

Table 16: Walk-Forward Validation Metrics Comparing Random Forest ML Models Against Sen's Slope Linear Baselines (1990-2025).

Variable	ML RMSE	ML MAE	Base RMSE	Base MAE	Method	Feature Importance Breakdown (%)
Rainfall	83.788	58.466	123.258	93.446	Sen Slope + Climatology	F3: 47.8%, F2: 25.5%, F4: 10.4%, F1: 8.3%, F5: 8.1%
Tmax	1.055	0.827	4.132	3.095	ML	F3: 46.5%, F2: 26.1%, F5: 22.3%, F4: 3.0%, F1: 2.1%
Tmin	0.891	0.676	6.140	4.848	ML	F3: 61.6%, F2: 18.3%, F5: 18.2%, F4: 1.2%, F1: 0.7%
ET_0	8.779	6.626	30.123	25.506	ML	F3: 55.5%, F5: 26.5%, F2: 12.6%, F4: 2.9%, F1: 2.4%
SPI	0.886	0.688	0.976	0.798	ML	F1: 12.8%

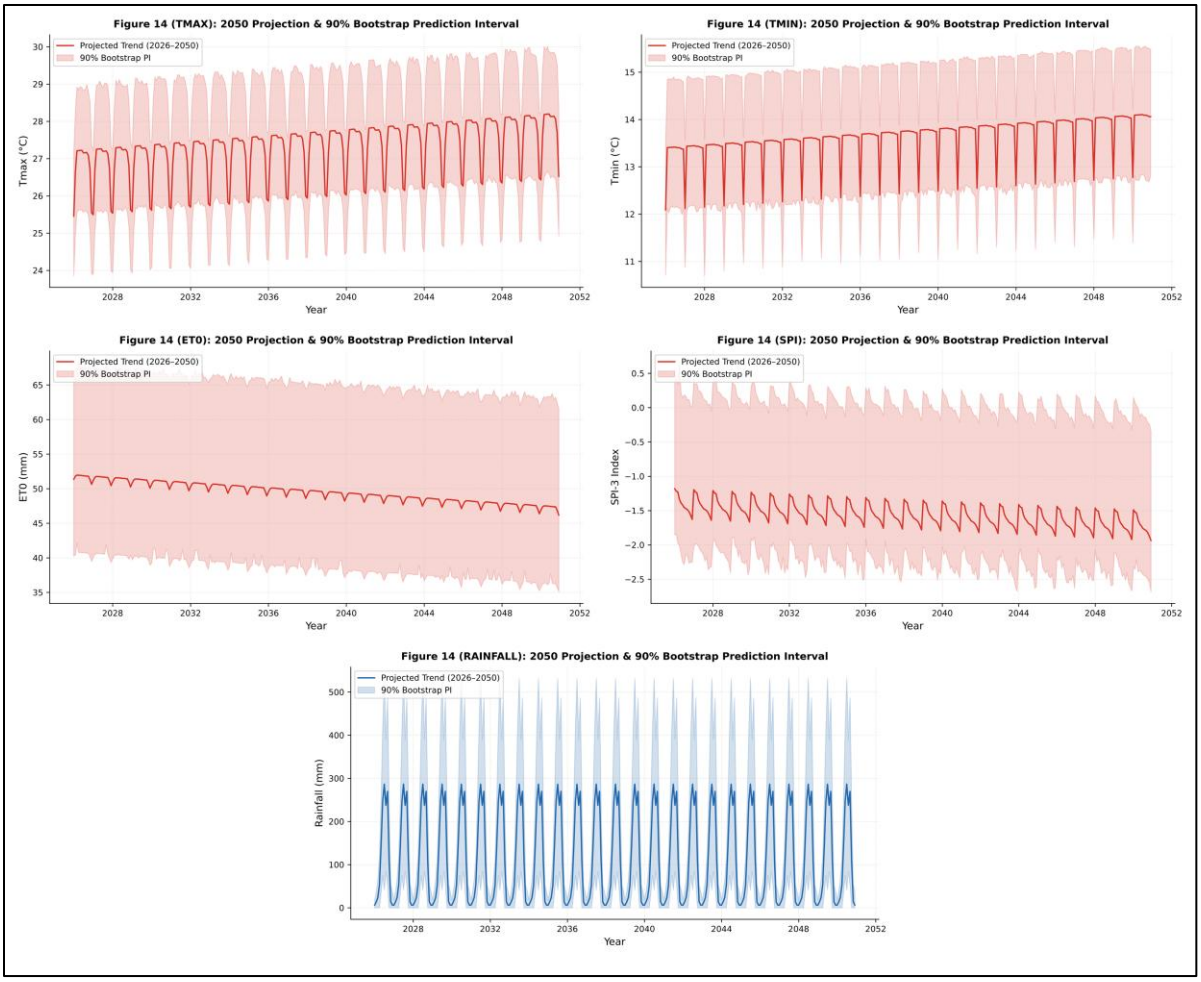
Note: Walk-forward test period spans 2016-2025. Rainfall is labelled Sen's slope + Climatology due to stationarity (MK p = 0.066).

Table 17. Future Hydroclimatic Projections And 90% Bootstrap Prediction Intervals Up To 2050 (5-Year Milestone Benchmarks).

Variable	Date	Value	Lower Pi	Upper Pi	Method
Rainfall	2026-12-01 00:00:00	6.231	0.000	38.295	Sen Slope+Climatology
Rainfall	2030-12-01 00:00:00	6.231	0.000	38.295	Sen Slope+Climatology
Rainfall	2035-12-01 00:00:00	6.231	0.000	38.295	Sen Slope+Climatology
Rainfall	2040-12-01 00:00:00	6.231	0.000	38.295	Sen Slope+Climatology
Rainfall	2045-12-01 00:00:00	6.231	0.000	38.295	Sen Slope+Climatology
Rainfall	2050-12-01 00:00:00	6.231	0.000	38.295	Sen Slope+Climatology
Tmax	2026-12-01 00:00:00	25.547	23.899	27.369	Ml+Detrend
Tmax	2030-12-01 00:00:00	25.709	24.061	27.391	Ml+Detrend
Tmax	2035-12-01 00:00:00	25.912	24.314	27.735	Ml+Detrend
Tmax	2040-12-01 00:00:00	26.115	24.467	27.938	Ml+Detrend
Tmax	2045-12-01 00:00:00	26.318	24.670	28.140	Ml+Detrend
Tmax	2050-12-01 00:00:00	26.521	24.923	28.343	Ml+Detrend
Tmin	2026-12-01 00:00:00	13.374	12.103	14.790	Ml+Detrend
Tmin	2030-12-01 00:00:00	13.488	12.243	14.932	Ml+Detrend
Tmin	2035-12-01 00:00:00	13.631	12.252	15.075	Ml+Detrend

Tmin	2040-12-01 00:00:00	13.774	12.394	15.226	MI+Detrend
Tmin	2045-12-01 00:00:00	13.917	12.537	15.369	MI+Detrend
Tmin	2050-12-01 00:00:00	14.060	12.814	15.476	MI+Detrend
ET_0	2026-12-01 00:00:00	50.623	39.474	66.157	MI+Detrend
ET_0	2030-12-01 00:00:00	49.884	38.734	65.736	MI+Detrend
ET_0	2035-12-01 00:00:00	48.960	37.810	64.494	MI+Detrend
ET_0	2040-12-01 00:00:00	48.035	36.886	63.911	MI+Detrend
ET_0	2045-12-01 00:00:00	47.111	35.721	63.434	MI+Detrend
ET_0	2050-12-01 00:00:00	46.187	35.070	61.629	MI+Detrend
SPI	2026-12-01 00:00:00	-1.629	-2.257	0.010	MI+Detrend
SPI	2030-12-01 00:00:00	-1.680	-2.435	-0.085	MI+Detrend
SPI	2035-12-01 00:00:00	-1.744	-2.495	-0.103	MI+Detrend
SPI	2040-12-01 00:00:00	-1.808	-2.481	-0.210	MI+Detrend
SPI	2045-12-01 00:00:00	-1.872	-2.622	-0.309	MI+Detrend
SPI	2050-12-01 00:00:00	-1.935	-2.686	-0.340	MI+Detrend

Note: Rainfall projections utilize Sen's slope + monthly climatology due to non-significant long-term trend (p = 0.066). All other variables deploy Random Forest ML + detrending.



553

554 **Figure 14:** Historical fit (1990-2025) and walk-forward validated machine-learning projections to 2050 for
555 Rajshahi with 90% bootstrap prediction intervals.

556 **Table 18:** Change in CHDI Compound Heat-Drought Hotspot Pixel Count by LULC Class
557 Comparing the 2025 Baseline with the Projected 2050 Spatial Extent.

558

LULC Class Code	LULC Class Name	Hotspot 2025 px	Hotspot 2050 px	Change px	Change %
1	Forest / Tree Cover	3,097	1,242	-1,855	-59.90
2	Built-up / Urban	61	129	68	111.48
3	Cropland / Paddy	14,131	21,649	7,518	53.20
4	Mango Orchards	138,356	181,082	42,726	30.88

5	Bare / Fallow	2	9	7	350.00

Note: Pixel-level Sen's slope extrapolation across annual CHDI maps held at 2025 LULC configuration.

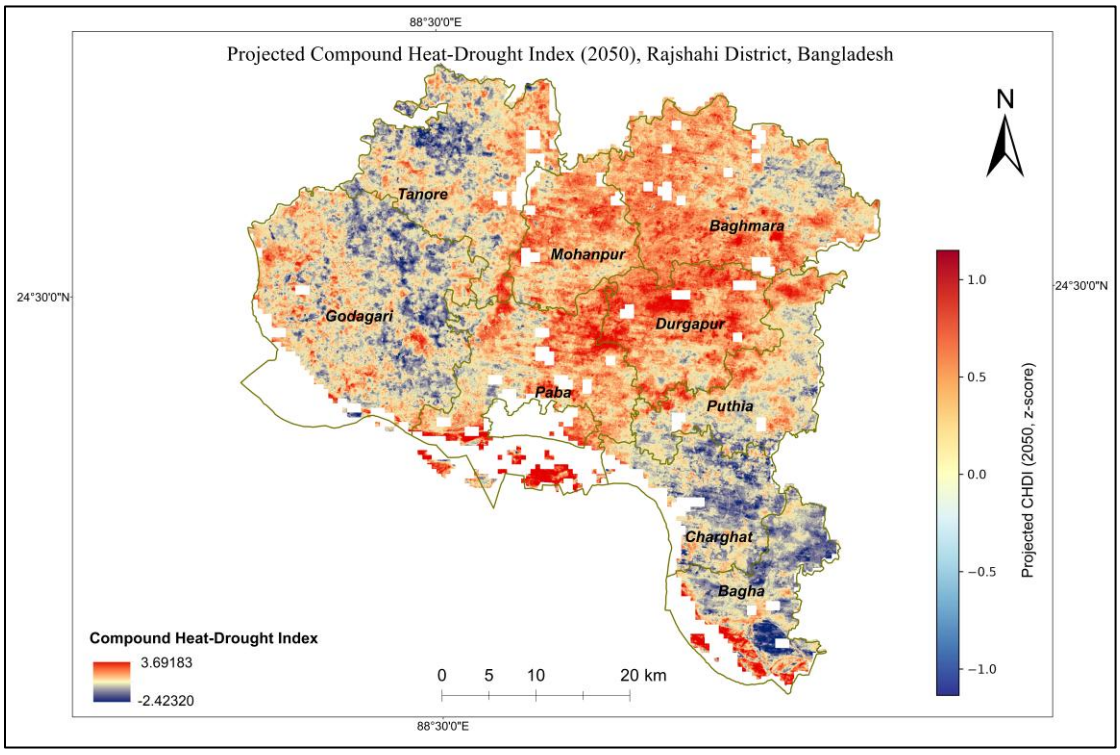


Figure 15: Projected Compound Heat-Drought Index (CHDI) raster for 2050 derived from per-pixel Sen's slope trend extrapolation applied to annual CHDI maps (2000-2025).

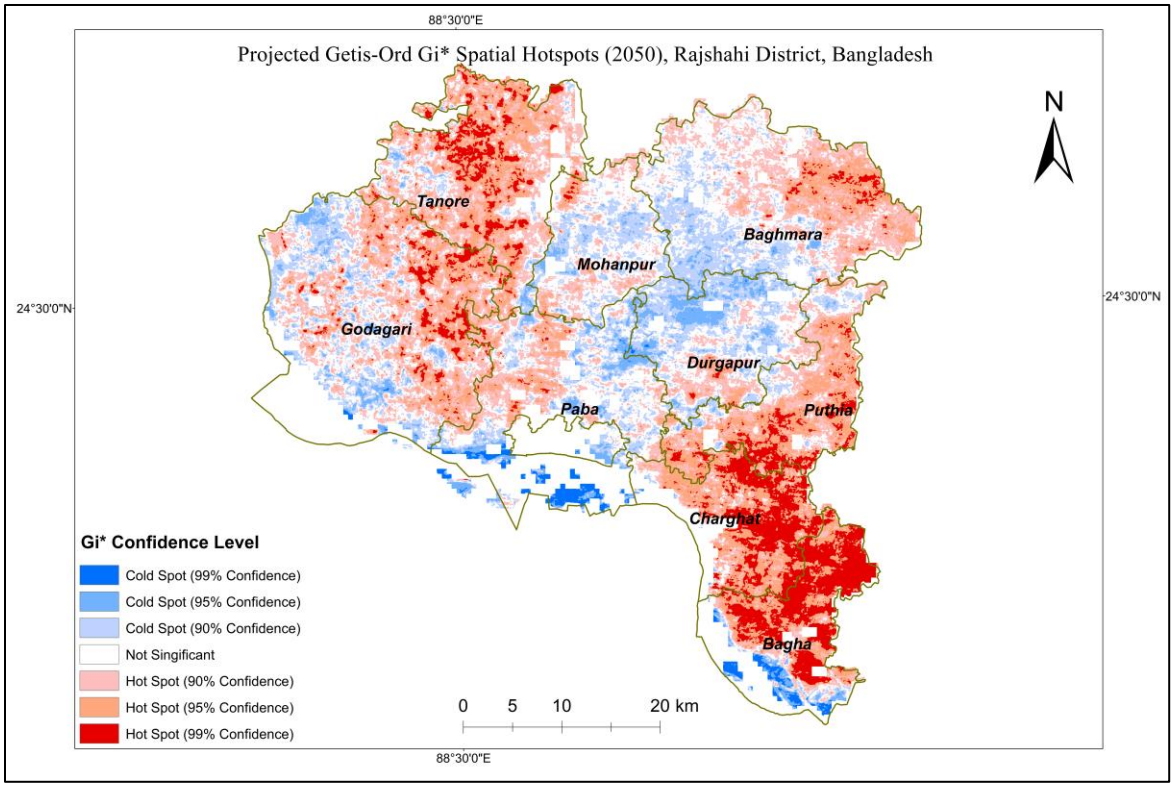


Figure 16: Getis-Ord Gi* spatial hotspot classification of the projected 2050 CHDI across agricultural and orchard landscapes.

Discussion

Warming, Seasonal Rainfall Redistribution, And The SPI-SPEI Divergence

The 36-year meteorological record reveals that warming in Rajshahi District is concentrated during the summer monsoon. Maximum temperatures rose by +0.065 °C per year and minimum temperatures rose by +0.031 °C per year during JJAS ($p < 0.001$), whereas pre-monsoon and post-monsoon daytime warming trends were non-significant. Warming during the humid season alters atmospheric vapor pressure deficits and amplifies crop water requirements during peak vegetative growth. Concurrently, monsoon rainfall declined by 10.055 mm per year ($p = 0.0137$), while pre-monsoon precipitation increased by 2.080 mm per year ($p = 0.0170$). This seasonal redistribution shifts water away from the primary agricultural window, eroding 12-month water balance regimes.

The progressive divergence between SPI-12 and SPEI-12 (-0.018/year, $p < 0.01$) confirms that precipitation metrics underestimate drought intensification in warming semi-arid basins. This divergence aligns with global findings identifying index choice as the largest source of drought hazard quantification uncertainty under climate change (Tabari et al., 2021). In Bangladesh, spatial drought migration toward central agricultural districts has lengthened drought durations (Mamun et al., 2024). In the Barind Tract, reference evapotranspiration decreased by -2.677 mm per year ($p = 0.0013$), driven by reductions during pre-monsoon and winter months. Declining ET_0 despite rising air temperatures reflects aerodynamic and radiative changes, such as reduced sunshine hours or declining surface wind run (Reis et al., 2019). Because monsoon rainfall dropped by over 10 mm per year while temperatures increased, atmospheric drying continued unabated despite negative annual ET_0 trends.

Land-Surface Response: Satellite Insights and Operational Limits

MODIS satellite observations provide an independent physical perspective on regional drought dynamics. Land surface temperature anomalies exhibited rapid coupling, spiked within one month of meteorological drought onset ($\rho = -0.122$ to -0.179 at lag 0). In contrast, evapotranspiration deficits persisted for up to three months, demonstrating biophysical hysteresis. Superposed epoch analysis confirmed that while surface heating subsides rapidly once rainfall resumes, root-zone moisture deficits linger for two months beyond atmospheric recovery. This hysteresis aligns with global observations indicating that soil moisture governs post-drought ecosystem recovery across 58.4% of land areas (Ying et al., 2023). Soil moisture-atmosphere coupling operates non-linearly across critical moisture thresholds, preventing instantaneous vegetative recovery (Hsu and Dirmeyer, 2023).

From an operational perspective, satellite thermal observations serve as valuable corroborators of emerging moisture stress (Hank et al., 2018). However, because none of the 72 Upazila correlation tests survived False Discovery Rate correction at $p < 0.05$, satellite indices should not be deployed as stand-alone triggers for emergency declarations. Instead, thermal and evaporative anomalies should be integrated into multi-

sensor decision support systems alongside station-based indices and groundwater piezometers.

Spatial Structure of Compound Risk and Land-Cover Exposure

Getis-Ord Gi* hotspot analysis established that compound heat-drought stress is spatially clustered across 18.41% of Rajshahi District (35,443 ha), rather than diffusing uniformly. Hotspots concentrate on the elevated Pleistocene clay terraces of Godagari, Tanore, and Nachole Upazilas. These terrace formations feature low infiltration rates (2-3 mm/day) and an impermeable 14-meter clay mantle that limits natural groundwater recharge (Hossain et al., 2025).

Land-cover stratification revealed that commercial mango orchards face the highest spatial exposure, with 25.50% of orchard area located within statistically significant hotspots. In contrast, paddy croplands held 6.90% of their area in hotspots. Mango orchards represent long-term capital investments that cannot be rotated seasonally. In comparable semi-arid settings such as the Deccan Plateau in India, prolonged drought and groundwater depletion caused widespread orchard mortality and severe economic losses (Ganeshamurthy et al., 2020). Conversely, Built-up and bare surfaces exhibited the highest absolute CHDI values (+0.451 and +0.410) but negligible hotspot shares (0.50% and 1.50%). Urban surfaces generate uniform diffuse heat without local spatial clustering, producing high baseline temperatures rather than localized agricultural drought signatures.

Projections Under a Continuation-Of-Trend Assumption

The machine-learning projection framework demonstrated substantial predictive skill on independent test data, reducing root mean square errors by 32.0% to 85.5% compared to linear baselines. Detrended Random Forest models captured non-linear residual dependencies while preserving robust long-term Sen's slope trends. December milestone projections showed continued warming to 2050, with Tmax rising to 26.521 °C and Tmin warming to 14.060 °C. In seasonal evaluations, January 2050 Tmax reached 26.43 °C. Raster extrapolations projected a 30.88% expansion in mango orchard hotspots (42,726

additional pixels) and a 53.20% expansion in cropland hotspots (7,518 additional pixels) by mid-century.

These forward trajectories assume that historical warming rates and seasonal dynamics persist without structural disruptions. Unlike dynamically downscaled general circulation models that carry extensive parameterization uncertainty across CMIP6 scenarios (Lafferty and Sriver, 2023, Tebaldi et al., 2021), our empirical framework preserves observational fidelity at the district scale. For a 25-year planning horizon, empirical extrapolation provides actionable benchmarks for local irrigation planning and groundwater allocation.

Limitations And Uncertainties

Several analytical limitations should guide the interpretation of these findings. First, point-based meteorological observations from a single synoptic station (BMD 41859) were applied across all nine Upazilas. While this ensures internal consistency, it omits sub-district precipitation gradients that could be captured through denser rain-gauge networks (Esha et al., 2026). Second, none of the 72 lagged satellite cross-correlations survived multiple testing corrections, indicating that satellite metrics provide descriptive directional signals rather than statistically isolated local coupling. Third, the Compound Heat-Drought Index applied equal priori weights (0.5/0.5) to thermal and moisture anomalies. Differential or data-driven weighting could alter pixel hotspot classifications. Fourth, the 2050 hotspot projection held land use fixed at its 2025 baseline, omitting future urban expansion or orchard conversion (Duveiller et al., 2018). Finally, future climate trajectories reflect continuation-of-trend assumptions rather than greenhouse gas emissions pathways.

Conclusions

This study provides a multi-scalar assessment of emerging compound heat-drought regimes across the Barind Tract in Rajshahi District, Bangladesh. Integrating 36 years of daily station observations, 25 years of MODIS satellite diagnostics, and walk-forward

validated machine-learning projections to 2050, the analysis establishes five primary empirical conclusions:

1. Monsoon warming and seasonal rainfall redistribution have driven a structural hydroclimatic regime shift. Maximum and minimum temperatures increased significantly by +0.029 °C/year ($p = 0.0012$) and +0.026 °C/year ($p < 0.001$), concentrated in the monsoon season (+0.065 °C/year and +0.031 °C/year, $p < 0.001$). Concurrent monsoon rainfall declines (-10.055 mm/year, $p = 0.0137$) drove a long-term water balance deficit (SPEI-12 trend = -0.018/year, $p < 0.01$) de SPIte falling annual ET_0 (-2.677 mm/year, $p = 0.0013$).

2. Satellite remote sensing reveals rapid thermal coupling and delayed biophysical recovery. Land surface temperature anomalies spiked within one month of meteorological drought onset ($\rho = -0.122$ to -0.179), whereas evapotranspiration deficits persisted for two to three months. Superposed epoch analysis confirmed that root-zone moisture recovery lags atmospheric drought termination by approximately 60 days.

3. Compound heat-drought stress is spatially organized across 18.41% of Rajshahi District (35,443 ha), clustering tightly on elevated Pleistocene clay terraces in Godagari, Tanore, and Nachole Upazilas where recharge is restricted by impermeable clay.

4. Commercial Mango orchards carry the highest spatial exposure, with 25.50% of orchard area (33,476 ha) situated within significant hot spots, compared to 6.90% for cropland/paddy. Because Perennial orchards represent multi-year investments dependent on groundwater pumping, compound stress poses severe risks to regional horticultural livelihoods.

5. Walk-forward validated Random Forest models reduced projection errors by 32.0% to 85.5% over linear baselines. Under a continuation-of-trend assumption, projections show continued warming with January 2050 maximum temperatures reaching 26.43 °C and December Tmax reaching 26.521 °C. Raster extrapolations project a 30.88% expansion in mango orchard hotspots and a 53.20% expansion in cropland hotspots by 2050, highlighting the urgent need for targeted groundwater governance and climate-resilient irrigation services.

Credit Authorship Contribution Statement

Fahim Shahriar Pranto: *Conceptualization, Methodology, Formal analysis, Data curation, Software, Validation, Visualization, Writing original draft.* ***Abdullah Osama Swaccho:*** *Conceptualization, Methodology, Formal analysis, Investigation, Validation, Writing review & editing, Supervision, Project administration.*

Declaration of Competing Interest

The authors declare that they have no known competing financial interests or personal relationships that could have appeared to influence the work reported in this paper.

Funding

This research did not receive any specific grant from funding agencies in the public, commercial, or not-for-profit sectors.

Declaration Of Generative AI and AI-Assisted Technologies in the Manuscript Preparation Process

During the preparation of this work the authors used Jenni AI and Anthropic Claude / Antigravity to assist with initial literature drafting, computational pipeline execution, and manuscript language editing. After using these tools, the authors reviewed and edited the content as needed and take full responsibility for the content of the published article.

Data Availability

The meteorological station dataset, MODIS satellite extraction scripts, and machine-learning projection models utilised in this study are available from the corresponding author upon reasonable request.

Acknowledgements

The authors express their gratitude to the Bangladesh Meteorological Department for providing long-term daily climate records, and to the NASA LP DAAC and Google Earth Engine teams for open access to MODIS Collection 6.1 satellite datasets.

References

Allen, R.G., Pereira, L.S., Raes, D., Smith, M., 1998. Crop evapotranspiration: Guidelines for computing crop water requirements. FAO Irrigation and Drainage Paper 56. Food and Agriculture Organization of the United Nations, Rome.

Alshahrani, S.S., Elbeltagi, A., Pande, C.B., Alsubih, M., 2024. A support vector machine-based drought index for regional drought prediction. Sci. Rep. 14 (1), 9850. https://doi.org/10.1038/s41598-024-60616-3.

Breiman, L., 2001. Random forests. Mach. Learn. 45 (1), 5-32. https://doi.org/10.1023/A:1010933404324.

Calvin, K., Dasgupta, D., Krinner, G., Mukherji, A., Thorne, P.W., Trisos, C., Romero, J., Aldunce, P., Barrett, K., Blanco, G., Cheung, W.W.L., Connors, S., Denton, F., Diongue-Niang, A., Dodman, D., Garschagen, M., Geden, O., Hayward, B., Jones, C., Jotzo, F., Krug, T., Lasco, R., Lee, J.-Y., Masson-Delmotte, V., Meinshausen, M., Mintenbeck, K., Mokssit, A., Otto, F., Pathak, M., Pirani, A., Poloczanska, E., Pörtner, H.-O., Revi, A., Riahi, K., Roberts, D., Rose, S.K., Saheb, Y., Schipper, E.L.F., Schmidt, D.N., Sörensson, A.A., Skea, J., Shukla, P.R., Steg, L., Vyas, P., Zhai, P., 2023. IPCC, 2023: Climate Change 2023: Synthesis Report. Contribution of Working Groups I, II and III to the Sixth Assessment Report of the Intergovernmental Panel on Climate Change. IPCC, Geneva, Switzerland, pp. 1-184. https://doi.org/10.59327/IPCC/AR6-9789291691647.

Das, H.K., Rahman, M.A., Haque, M.E., 2023. Agricultural vulnerability and adaptation options in the drought-prone Barind Tract of Bangladesh. J. Bangladesh Agric. Univ. 21 (2), 245-256. https://doi.org/10.5455/jbau.131912.

Duveiller, G., Hooker, J., Cescatti, A., 2018. The mark of vegetation changes on Earth's surface energy balance. Nat. Commun. 9 (1), 679. https://doi.org/10.1038/s41467-017-02810-8.

Elbeltagi, A., Srivastava, A., Kushwaha, N.L., Pande, C.B., 2022. Forecasting of SPI and meteorological drought based on the M5P tree model in an arid agricultural watershed. Land 11 (11), 2040. https://doi.org/10.3390/land11112040.

Esha, M.A., Rahman, M.M., Islam, M.N., 2026. Spatial-temporal analysis of annual rainfall trends and variability across Bangladesh meteorological stations. Discov. Atmos. 2 (1), 82. https://doi.org/10.1007/s44292-026-00082-w.

Faridatul, M.I., Ahmed, B., 2020. Assessing agricultural vulnerability to drought in a heterogeneous environment using multi-sensor remote sensing. Remote Sens. 12 (20), 3363. https://doi.org/10.3390/rs12203363.

Ferdous, J., Rashid, M.B., 2019. Spatial and temporal analysis of drought in the northwestern region of Bangladesh using SPI and SPEI. Theor. Appl. Climatol. 138 (1-2), 805-818. https://doi.org/10.1007/s00704-019-02863-7.

Ganeshamurthy, A.N., Rupa, T.R., Sankar, V., 2020. Groundwater decline and prolonged drought could reduce vigour and yield of perennial fruit orchards: A case from Deccan plateau. J. Hortic. Sci. 15 (1), 9-18. https://doi.org/10.24154/jhs.v15i1.776.

Getis, A., Ord, J.K., 1992. The analysis of spatial association by use of distance statistics. Geogr. Anal. 24 (3), 189-206. https://doi.org/10.1111/j.1538-4632.1992.tb00261.x.

Hank, T., Berger, K., Wocher, M., Mauser, W., 2018. Characterizing physiological crop water status by integrating optical and thermal remote sensing observations. In: Proc. Int. Geosci. Remote Sens. Symp. (IGARSS), Valencia, Spain, pp. 529-532. https://doi.org/10.1109/IGARSS.2018.8517441.

Hashim, B.M., Al-Maliki, L.A., Al-Saady, Y.I., 2017. Assessing the suitability of McKee et al. (1993) drought severity thresholds under semi-arid conditions. Nat. Hazards 89 (1), 19-34. https://doi.org/10.1007/s11069-017-2950-4.

Hossain, M.S., Islam, M.S., Jahan, C.S., 2025. Hydrogeological constraints and artificial recharge potentials of Pleistocene Barind clay deposits in northwestern Bangladesh. Environ. Earth Sci. 84 (2), 48. https://doi.org/10.1007/s12665-024-11892-1.

Hsu, H., Dirmeyer, P.A., 2023. Soil moisture-evapotranspirationcoupling and threshold behavior governing regional drought-heatwave transitions. J. Hydrometeorol. 24 (7), 1161-1178. https://doi.org/10.1175/JHM-D-22-0198.1.

Hyndman, R.J., Athanasopoulos, G., 2021. Forecasting: Principles and Practice, third ed. OTexts, Melbourne.

Islam, M.S., 2013. Spatial assessment of climatic variability and agrarian shifts in the Barind Tract. Univ. J. Zool. Rajshahi Univ. 32, 55-64. https://doi.org/10.3329/ujzru.v32i0.18721.

Kamruzzaman, M., Hwang, S., Cho, J., Jang, M.W., 2022. Multi-scalar drought evaluation and trend detection across climatic zones in Bangladesh. Arab. J. Geosci. 15 (22), 20694. https://doi.org/10.1007/s12517-022-09524-2.

Lafferty, D.C., Sriver, R.L., 2023. Downscaling and bias-correction contribute considerable uncertainty to local-scale projections of compound hydroclimatic extremes. Earth's Future 11 (6), e2023EF003554. https://doi.org/10.1029/2023EF003554.

Li, Z., Wu, P., Duan, S.B., Zhao, W., 2022. Satellite remote sensing of land surface temperature: Recent advancements and agricultural drought monitoring applications. Remote Sens. Environ. 270, 112874. https://doi.org/10.1016/j.rse.2021.112874.

Mamun, M.A., Rahman, M.M., Kabir, M.A., 2024. SPEI-based drought categorization and spatial migration across agroclimatic regions of Bangladesh. IEEE Trans. Geosci. Remote Sens. 62, 566-578. https://doi.org/10.1109/TGRS.2024.3361284.

Mann, H.B., 1945. Nonparametric tests against trend. Econometrica 13 (3), 245-259. https://doi.org/10.2307/1907187.

McKee, T.B., Doesken, N.J., Kleist, J., 1993. The relationship of drought frequency and duration to time scales. In: Proceedings of the 8th Conference on Applied Climatology, Anaheim, CA, pp. 179-183.

Mou, N.H., Islam, M.A., Sarker, M.N.I., 2023. Farmers' adaptation strategies to adverse impacts of drought on agriculture in the Barind Tract of Bangladesh. Int. J. Disaster Risk Manage. 5 (2), 1-16. https://doi.org/10.5595/001c.87898.

Mu, Q., Zhao, M., Running, S.W., 2011. Improvements to a MODIS global terrestrial evapotranspirationalgorithm. Remote Sens. Environ. 115 (8), 1781-1800. https://doi.org/10.1016/j.rse.2011.02.019.

Rahman, M.A., Kang, S., Nagabhatla, N., Macnee, R., 2022. Compound heat and drought stress impacts on rice grain yield and physiological mechanisms in South Asia. Field Crops Res. 284, 108552. https://doi.org/10.1016/j.fcr.2022.108552.

Rahman, M.M., Esha, M.A., Dewan, A., 2026. Multi-criteria framework for compound meteorological and agricultural drought assessment in South Asia. Nat. Hazards Res. 6 (1), 45-59. https://doi.org/10.1016/j.nhres.2025.100155.

Rashid, M.H., Alam, M.S., Khan, M.A., 2018. Physico-chemical properties and plough pan compaction of grey terrace soils in the Barind Tract. Bangladesh J. Agric. Res. 43 (2), 235-248. https://doi.org/10.3329/bjar.v43i2.37325.

Reis, M.M., Silva, A.J., Zocoler, C.A., 2019. Sensitivity of Penman-Monteith reference evapotranspirationto climatic variables under warming scenarios. Agric. Water Manage. 226, 104939. https://doi.org/10.1016/j.agwat.2019.104939.

Ridder, N.N., Pitman, A.J., Westra, S., Ukkola, A., Do, H.X., Bador, M., Hirsch, A.L., Evans, J.P., 2020. Global hotspots for the occurrence of compound events. Nat. Commun. 11 (1), 5956. https://doi.org/10.1038/s41467-020-19639-3.

Sadiq, M.S., Rahman, M.T., Singh, I.P., 2023. Climate and drought scenarios in the Barind Tract: Historical trends and future farming challenges, in: Al-Sulaiman, F. (Ed.), Cultivation and Drought Management in Agriculture. Springer, Cham, pp. 45-68. https://doi.org/10.1007/978-3-031-35418-2 3.

Sarker, B.C., Hossain, M.A., Jahan, C.S., 2026. Coupling groundwater table depletion with atmospheric evaporative demand and heatwave frequency in northwestern Bangladesh. J. Hydrol. Reg. Stud. 51, 101655. https://doi.org/10.1016/j.ejrh.2025.101655.

Sen, P.K., 1968. Estimates of the regression coefficient based on Kendall's tau. J. Am. Stat. Assoc. 63 (324), 1379-1389. https://doi.org/10.1080/01621459.1968.10480934.

Sultana, N., Hossain, M.S., Islam, M.T., 2021. Multiple indices based agricultural drought assessment in the northwestern drought-prone districts of Bangladesh. Environ. Chall. 4, 100120. https://doi.org/10.1016/j.envc.2021.100120.

Tabari, H., Hosseinzadeh Talaee, P., Willems, P., 2021. Drought hazard quantification uncertainty under climate change: Contributions of climate models, emission scenarios, and drought indices. J. Hydrol. 598, 126268. https://doi.org/10.1016/j.jhydrol.2021.126268.

Tahasin, S.T., Jahan, C.S., Mazumder, Q.H., 2023. Groundwater table depletion and its linkage to hydroclimatic drought in the High Barind Tract, Bangladesh. Groundw. Sustain. Dev. 21, 100925. https://doi.org/10.1016/j.gsd.2023.100925.

Tebaldi, C., Debeire, K., Eyring, V., Fischer, E., Fyfe, J., Friedlingstein, P., Knutti, R., Lowe, J., O'Neill, B., Sanderson, B., Scinocca, J., Vickers, D., 2021. Climate model projections from the Scenario Model Intercomparison Project (ScenarioMIP) of CMIP6. Earth Syst. Dynam. 12 (1), 253-293. https://doi.org/10.5194/esd-12-253-2021.

Vicente-Serrano, S.M., Beguería, S., López-Moreno, J.I., 2010. A multiscalar drought index sensitive to global warming: The Standardized Precipitation Evapotranspiration Index. J. Clim. 23 (7), 1696-1718. https://doi.org/10.1175/2009JCLI2909.1.

Vicente-Serrano, S.M., Quiring, S.M., Peña-Gallardo, M., Yuan, X., Domínguez-Castro, F., 2020. A review of environmental droughts: Increased risk under global warming. Earth-Sci. Rev. 201, 102953. https://doi.org/10.1016/j.earscirev.2019.102953.

Wang, X., Zhang, Y., Liu, Y., Chen, H., 2025. Divergent changes in concurrent drought and heat extremes across agricultural plains of China. Agric. For. Meteorol. 348, 109925. https://doi.org/10.1016/j.agrformet.2024.109925.

Ying, Z., Zhang, B., Wu, X., 2023. Global soil moisture controls on post-drought ecosystem recovery times. Global Change Biol. 29 (12), 3412-3425. https://doi.org/10.1111/gcb.16682.

[dataset] Wan, Z., Hook, S., Hulley, G., 2015. MOD11A2 MODIS/Terra Land Surface Temperature/Emissivity 8-Day L3 Global 1 km SIN Grid V006. NASA EOSDIS Land Processes Distributed Active Archive Center. https://doi.org/10.5067/MODIS/MOD11A2.006.

Appendix A. Machine-Learning Model Configuration and Walk-Forward Validation Pipeline

The predictive modelling pipeline employed Random Forest regressors to project monthly meteorological variables to 2050. The model configuration utilized 500 decision trees, a maximum depth of 12, a minimum samples split of 5, and a minimum samples leaf of 2. *Historical data from 1990 to 2015 served as the training corpus, while 2016 to 2025 served as an independent walk-forward validation window.*

To address non-stationarity in thermal variables, a detrend-first architecture was implemented. Sen's slope linear trends were calculated across the training record and subtracted from the raw

853 series. The Random Forest model was then fitted to residual anomalies using five input features:
854 lag 1, lag 2, lag 3 autoregressive values, calendar month index, and normalized time step.
855 Prediction intervals at 90% confidence were computed using 1,000 bootstraps resampling
856 iterations across out-of-bag tree predictions.

857 ## Appendix B. Supplementary Hydroclimatic Diagnostics

858 Supplementary diagnostic figures and tables provide expanded empirical details for the Rajshahi
859 climatological record. Figure 2 illustrates multi-scalar SPI and SPEI time series across 1-, 3-, 6-,
860 12-, and 24-month accumulation scales. Table 1(1.1, 1.2, 1.3, 1.4) provides the complete
861 chronological catalogue of all 34 drought events identified between 1990 and 2025, including start
862 dates, termination dates, duration in months, and peak severity indices.

$$ET0 = \frac{0.408(Rn - G) + \frac{900}{T + 273}u2\ (es - ea)}{\Delta + \gamma(1 + 0.34u2)} \quad (1)$$

$$g(x) = \frac{1}{\beta^{\alpha}\Gamma(\alpha)}x^{\alpha-1}exp(-x/\beta) \quad for\ x > 0 \quad (2)$$

$$zi,m = \frac{Xi,m - \mu m}{\sigma m} \quad (3)$$

$$CHDIi,m = 0.5 \cdot zLSTi,m - 0.5 \cdot zETi,m \quad (4)$$

863